Cellular and Molecular Life Sciences (2024) 81:12
https://doi.org/10.1007/s00018-023-05064-4

Cellular and Molecular Life Sciences

ORIGINAL ARTICLE

Mitochondrial impairment, decreased sirtuin activity and protein acetylation in dorsal root ganglia in Friedreich Ataxia models

Arabela Sanz-Alcázar[1] · **Elena Britti**[1] · **Fabien Delaspre**[1] · **Marta Medina-Carbonero**[1] · **Maria Pazos-Gil**[1] · **Jordi Tamarit**[1] · **Joaquim Ros**[1] · **Elisa Cabiscol**[1]

Received: 17 May 2023 / Revised: 16 November 2023 / Accepted: 25 November 2023 / Published online: 21 December 2023

Abstract

Friedreich ataxia (FA) is a rare, recessive neuro-cardiodegenerative disease caused by deficiency of the mitochondrial protein frataxin. Mitochondrial dysfunction, a reduction in the activity of iron-sulfur enzymes, iron accumulation, and increased oxidative stress have been described. Dorsal root ganglion (DRG) sensory neurons are among the cellular types most affected in the early stages of this disease. However, its effect on mitochondrial function remains to be elucidated. In the present study, we found that in primary cultures of DRG neurons as well as in DRGs from the FXN^{I151F} mouse model, frataxin deficiency resulted in lower activity and levels of the electron transport complexes, mainly complexes I and II. In addition, altered mitochondrial morphology, indicative of degeneration was observed in DRGs from FXN^{I151F} mice. Moreover, the NAD$^+$/NADH ratio was reduced and sirtuin activity was impaired. We identified alpha tubulin as the major acetylated protein from DRG homogenates whose levels were increased in FXN^{I151F} mice compared to WT mice. In the mitochondria, superoxide dismutase (SOD2), a SirT3 substrate, displayed increased acetylation in frataxin-deficient DRG neurons. Since SOD2 acetylation inactivates the enzyme, and higher levels of mitochondrial superoxide anion were detected, oxidative stress markers were analyzed. Elevated levels of hydroxynonenal bound to proteins and mitochondrial Fe^{2+} accumulation was detected when frataxin decreased. Honokiol, a SirT3 activator, restores mitochondrial respiration, decreases SOD2 acetylation and reduces mitochondrial superoxide levels. Altogether, these results provide data at the molecular level of the consequences of electron transport chain dysfunction, which starts negative feedback, contributing to neuron lethality. This is especially important in sensory neurons which have greater susceptibility to frataxin deficiency compared to other tissues.

Keywords FXNI151F mice model · Sensory neurons · SirT3 · Redox state, mitochondrial dysfunction · Honokiol

Abbreviations

DRG	Dorsal root ganglia
ECAR	Extracellular acidification rate
ETC	Electron transport chain
FA	Friedreich ataxia
HNE	4-Hydroxynonenal
OCR	Oxygen consumption rate
SOD2	Mn-superoxide dismutase
ROS	Reactive oxygen species

✉ Elisa Cabiscol
elisa.cabiscol@udl.cat

Arabela Sanz-Alcázar
arabela.sanz@udl.cat

Elena Britti
elenabritti@hotmail.it

Fabien Delaspre
fabien.delaspre@udl.cat

Marta Medina-Carbonero
mmedinacarbonero@health.ucsd.edu

Maria Pazos-Gil
maria.pazos@udl.cat

Jordi Tamarit
Jordi.tamarit@udl.cat

Joaquim Ros
Joaquim.ros@udl.cat

[1] Departament de Ciències Mèdiques Bàsiques, Facultat de Medicina, Universitat de Lleida, IRBLleida, Edifici Biomedicina I, Av. Rovira Roure, 80, 25198 Lleida, Catalonia, Spain

Introduction

Frataxin is a mitochondrial protein that, at concentrations below 40% of normal levels, leads to Friedreich ataxia (FA), a disease caused by the presence of large expansions of GAA triplet repeats in the first intron of the frataxin (FXN) gene, which results in a low transcription rate and, consequently, diminished frataxin expression [1]. While triplet expansions in homozygosis are the most observed genetic abnormality in FA patients, 4% of them are compound heterozygotes displaying GAA repeats in one allele and point mutations in the other [2]. Decreased expression of frataxin is associated with mitochondrial dysfunction, iron and calcium imbalance, and increased oxidative stress. The function of frataxin and the mechanisms causing such cellular disturbances are not completely understood but it has been shown to regulate the activity of cysteine desulfurase, an enzyme required for the biosynthesis of iron–sulfur clusters [3]. Although it is generally accepted that frataxin activates iron–sulfur biogenesis in eukaryotes, iron–sulfur deficiency is not a universal consequence of frataxin deficiency, suggesting that the role of frataxin in this process is not essential [4].

Patients with FA suffer progressive limb and gait ataxia, dysarthria, reduced tendon reflex, extensor plantar responses and loss of position and vibration senses. Although much research has been conducted [5], there is no effective cure for the disease. The pathologic changes occur first in dorsal root ganglia (DRG) with loss of large sensory neurons, followed by degeneration of the spinocerebellar and corticospinal tracts [6]. DRG neurons express the highest levels of frataxin and display high vulnerability to frataxin down-regulation. For this reason, the consequences of frataxin depletion have been studied, at the histological level, in DRGs using conditional knockout mice [7] and samples from patients with FA [8, 9] Also, using primary cultures of frataxin-deficient DRG neurons, our group observed alterations of several parameters such as a decrease in mitochondrial membrane potential, increased fodrin cleavage by calpain and caspase, and Bax induction [10, 11]. These events led to apoptotic cell death that was rescued either by supplementing cultures with calcium chelators such as BAPTA or with TAT-BH4, the antiapoptotic domain of Bcl-xL fused to TAT peptide [10]. Besides apoptosis, ferroptosis is a process of cell death involving iron accumulation, lipid peroxidation and decreased GPX4 activity, among other factors [12] that has also been described in several models of FA [13, 14].

Our group has previously reported that, in frataxin-deficient cardiomyocytes and in DRG neurons, opening of the mitochondrial permeability transition pore occurred [15] and can be triggered by, among other causes, increased acetylation of the mitochondrial cyclophilin D (CypD) due to impairment of SirT3 function, the most abundant mitochondrial sirtuin [16], 17. SirT3 belongs to the sirtuin family, which are NAD-dependent class III histone deacetylases (HDAC). It is synthesized as a 44-kDa precursor that, once processed by mitochondrial proteases, is converted to a mature form of 28 kDa [18]. Although Sirt4 and Sirt5 have also been found in mitochondria [19], their deacetylase activity is very weak compared to that of SirT3 [20]. For this reason, SirT3 is the main sirtuin responsible for controlling the lysine acetylation levels of mitochondrial proteins [21]. In this context, SirT3 has been involved in the control of mitochondrial fatty acid oxidation, and regulates the activity of succinate dehydrogenases, pyruvate dehydrogenase as well as tricarboxylic acid cycle enzymes such as aconitase, isocitrate dehydrogenase and malate dehydrogenase [22–24]. In the electron transport chain (ETC), several proteins from complexes I to V are SirT3 targets [19]. Protein acetylation has been observed in the heart of a cardiac mouse model of FA and increases with age. Acetyl-SOD2 was identified as one of the targets; the acetylated form is inactive and, as a result, ROS production increases. Higher acetylation was associated with impaired mitochondrial fitness, altered lipid metabolism, and a decline in heart function as well as the development of steatosis and cardiac fibrosis [25]. SirT3 activators have thus been tested as a possible strategic therapy. Among them, resveratrol (an SirT3 activator [26] that increases SirT3 levels) was suggested as a possible therapy for FA a few years ago [5] and is now in phase 2 trials. Honokiol, another SirT3 activator, has anti-inflammatory, anti-tumor, anti-oxidative, and neuroprotective properties [27]. It has proven to be effective at, among other functions, reducing SOD2 acetylation, thus maintaining SOD2 activity under doxorubicin-induced oxidative stress [28].

In the current study, we analyzed the consequences of frataxin deficiency in DRG neurons using two models: primary cultures of frataxin-deficient DRGs and DRGs from the new mouse model FXN^{I151F} [29]. This mouse carries the I151F point mutation, equivalent to the human I154F pathological mutation. FXN^{I151F} homozygous mice present very low frataxin levels, biochemical alterations, and neurological deficits (starting at 23 weeks of age) that mimic those observed in patients with FA. Briefly, the FXN^{I151F} mice present reduced weight gain from 15 weeks of age onward, and they showed decreased: (i) motor coordination ability, assessed on a rotarod treadmill, (ii) forelimb strength, tested using a hanging-wire test, (iii) locomotor activity, performed using an open-field beam-breaker activity monitor and, (iv) gait ataxia, using paw print analysis [29]. In the present study, we detected a deficiency of mitochondrial respiration, which resulted in a decreased NAD^+/NADH ratio and, as a consequence, a decline in sirtuin activity. Mitochondrial

SOD2, a SirT3 substrate, showed increased levels of its acetylated (inactive) form, leading to oxidative stress. Interestingly, restored mitochondrial function and a decrease in both SOD2 acetylation and mitochondrial superoxide levels were observed in cells supplemented with honokiol, a SirT3 activator. These results indicate that a negative feedback mechanism involving decreased SirT3 activity contributes to neuron lethality in frataxin-deficient DRGs.

Materials and methods

Animals and isolation of DRGs from FXN^{I151F} mouse model

All experimentation with animals was performed according to the National Guidelines for the regulation of the use of experimental laboratory animals issued by the Generalitat de Catalunya and the Government of Spain (article 33.a 214/1997), which comply with the ARRIVE guidelines. Experimental protocols were evaluated and approved by the Experimental Animal Ethical Committee of the University of Lleida (CEEA). All procedures were performed at the animal facility. For euthanasia of animals, the guidelines of the American Veterinary Medical Association (AVMA) were followed. Male and female Sprague–Dawley rats (RRID:RGD_70508) were maintained in standard conditions of 12-h cycles of light and dark, a constant temperature of 20 °C and eating and drinking ad libitum.

FXN^{I151F} heterozygous mice (C57BL/6 J-Fxnem10(T146T,I151F)Lutzy/J) were obtained from the Jackson Laboratory, Bar Harbor, ME, USA (Stock Number 31922) as previously described [29]. Intercrosses of heterozygous animals were performed to generate the homozygous WT and FXN^{I151F} mice. Animals were housed in standard ventilated cages with 12 h light/dark cycles and fed with a normal chow diet ad libitum. Animals were weighed weekly. Genotyping was performed by sequencing a PCR product amplified from DNA extracted from tail biopsy specimens as described previously [29].

For DRG isolation, animals were sacrificed by cervical dislocation at 21 or 39 weeks of age. In brief, the spinal column was excised from the base of the skull to just caudal to the femurs. After the spinal column had been cut, fat and other tissues or nerves outside the column were removed. The spinal column was divided in half by making a cut in the middle to improve access to the DRGs. From this step, the dissection was performed with ice-cold PBS into a petri dish with a black base to facilitate the visualization of DRGs. The spinal cord was removed from the column and DRGs were located between each vertebra. DRGs were carefully extracted individually with forceps to prevent damage to the ganglia. Lumbar, thoracic and cervical DRGs were collected and axons were detached as far as possible. Pictures were taken at different steps of isolation (Supplementary Fig. 1). A more detailed explanation (including videos) is described in ref [30]. Once dissected, DRGs were collected into a cryotube, snap-frozen immediately in liquid nitrogen and stored at -80ºC. In a typical DRG isolation, we obtained around 30–40 ganglia from one mouse, which, once homogenized, gave an average yield of 200 ± 100 µg of protein.

Isolation and culture of primary rat DRG sensory neurons

For primary culture of DRG neurons, DRG were extracted from neonatal Sprague–Dawley rats (P3–P4) and purified as described [10, 11] with modifications. The ganglia (without the nerve roots) were dissociated by incubation in 0.025% trypsin (Sigma-Aldrich) without EDTA in GHEBS (137 mM NaCl, 2.6 mM KCl, 25 mM glucose, 25 mM HEPES, 100 µg/mL penicillin/streptomycin) for 30 min. Ganglia were then gently disrupted using a pipette to obtain a single cell suspension in Neurobasal culture media (GIBCO, Cat# 21,103,049) enriched with 2% horse serum (GIBCO, Cat# 16,050–122), 2% B27 Supplement (ThermoFisher Scientific, Cat#17,504–044), 0.5 mM L-glutamine (GIBCO, Cat# 25,030–024), 100 U/mL penicillin plus 100 ng/mL Streptomycin (GIBCO, Cat# P4458). Aphidicolin (Sigma–Aldrich, Cat# A0781) was added at a final concentration of 3.4 mg/mL to prevent the growth of non-neuronal cells and supplemented with 50 ng/mL murine β-nerve growth factor (PeproTech, Cat# 450–34) with 3 mg/mL DNAse I grade II (Roche, Cat# 104,159). The cell suspension was centrifuged at 1,300 rpm for 5 min with 7.5% BSA solution (Sigma, Cat# A8412). After 1 h of pre-plating in a p60 tissue dish (Corning Incorporated, Cat# 35,004) at 37 ℃/5%CO_2, the cells were then plated in tissue dishes pretreated with 0.1 mg/mL of collagen (Sigma, Cat# C7661-25) at a cell density of 14,000 cells/well. After 1–2 days, lentivirus transduction was performed with shRNA sequences targeting frataxin mRNA as described previously [31]. The RefSeq used was NM-008044, which corresponds to mouse frataxin. The clones used were TRCN0000197534 and TRCN0000006137 (here referred to as FXN1, FXN2). The vector SHC002, a non-targeted scrambled sequence, served as a control (Scr). Lentivirus particles (20 ng/1,000 cells) were added and replaced with fresh medium 6 h later. Experiments were performed after 1, 3 or 5 days as indicated. Neuronal survival was measured with a × 16 lens and cross-marked wells as described [10].

Mitochondrial respiration in primary cultures of DRG neurons

Oxygen consumption rate (OCR) and extracellular acidification rate (ECAR) were measured in primary cultures of DRG neurons using the Seahorse XFp analyzer (Agilent). DRG neurons were cultured (1, 3 and 5 days after lentivirus transfection) in Seahorse XF cell culture plates (103,726–100) pre-treated with collagen. One hour before the assay, the culture medium was changed to DMEM (Dulbecco's modified Eagle's medium, pH 7.4) with 2 mM glutamine, 1 mM pyruvate, and 10 mM glucose, the plates were placed in a 37 ℃ non-CO_2 incubator, and OCR and ECAR were measured according to the manufacturer's instructions. Mitochondrial complex inhibitors were sequentially injected into each well: oligomycin (1.5 µM) to inhibit complex V, FCCP (3 µM) as an uncoupling agent, and rotenone-antimycin A (0.5 µM each) to inhibit complexes I and III. All data were automatically calculated, recorded, and plotted using the Seahorse analytics software, and normalized by protein concentration per well. To study the role of SirT3, 2 µM honokiol was added to primary cultures 0 and 3 days after lentivirus transduction, and cellular respiration was analyzed using Seahorse XFp analyzer 48 h later.

Enzymatic activity of mitochondrial respiratory complexes

DRGs isolated from WT and FXN^{I151F} mice were homogenized with a Dounce homogenizer (ten strokes) in 50 mM Tris–HCl, 0.15 M KCl, pH 7.4 and gently sonicated. The homogenate was centrifuged (800×*g* for 15 min) and the supernatants were used to assay CoQ-dependent respiratory chain activities (CI + III and CII + III) as previously described [32] with minor modifications. To assess complex I + III activity, the rate of cytochrome c reduction was measured at 550 nm, using NADH as the electron donor. The sample was incubated in 50 mM Tris–HCl, 0.15 M KCl, pH 7.4 containing 1 mg/mL BSA, 40 µM cytochrome c and 240 µM KCN. After 2–3 min, 0.8 mM NADH was added, and cytochrome c reduction was recorded for another 2–3 min. The same procedure was performed in the presence of 4 µM rotenone (a complex I inhibitor) to determine the rotenone-sensitive reduction of cytochrome c. To check the activity of complex II + III, the sample was incubated for 10 min with 50 mM Tris–HCl, 0.15 M KCl, pH 7.4 plus 2 mM EDTA, 1 mg/mL BSA, 240 µM KCN, 4 µM rotenone and 10 mM succinate as a substrate. The reaction was initiated by addition of 40 µM cytochrome c and the decrease in absorbance was monitored at 550 nm for 2–3 min. The assay was also performed in the presence of 0.5 mM 2-thenoyltrifluoroacetone, a complex II inhibitor. In both assays (complex I + III and complex II + III), the results were expressed in nmol reduced cyt c/min/mg prot. Citrate synthase activity was measured with a coupled assay to reduce 5,5′-dithiobis-(2-nitrobenzoic acid) (DTNB) [33]. Briefly, DRG extracts obtained as described above were centrifuged at 12,000 rpm for 10 min and supernatants were added to 100 mM Tris–HCl pH 8.1 with 0.4 mg/mL DTNB and 10 mg/mL acetyl-CoA. Absorbance was measured at 412 nm for 2 min. Then, 8.5 mg/mL of oxaloacetate were added to the cuvette and the absorbance was measured again at 412 nm for 2 min for the detection of reduced DTNB. All spectrophotometric measurements were performed in 0.1-mL cuvettes using a double beam spectrophotometer (Shimadzu UV-160).

Western blot analysis

To obtain homogenates from primary cultures, DRG neurons were lysed (at day 5 after lentivirus transduction) with 2% SDS, 125 mM Tris–HCl pH 7.4, plus protease inhibitor cocktail (Roche), phosphatase inhibitor (Roche), and 5 µM trichostatin A (TSA, Sigma). Cell extracts were sonicated, heated at 95 ℃ for 5 min and centrifuged at 10,000 rpm for 10 min. Protein concentration was measured using the microBCA method (Thermo Scientific). To obtain tissue homogenates, isolated DRGs were placed in 1.5 mL screw cap polypropylene tubes in the presence of lysis buffer consisting of 50 mM Tris–HCl pH 7.5 containing a protease inhibitor cocktail (Roche). Glass beads (0.5–1.0 mm) were added to the mixture, which was then homogenized in a BioSpec Mini-Beadbeater. Following homogenization, SDS was added to a final concentration of 4%. This homogenate was vortexed for 1 min, heated at 98 ℃ for 5 min, sonicated and subsequently centrifuged at 12,000 × *g* for 10 min. Protein content in the supernatant was quantified using the BCA assay (Thermo Scientific).

Protein extracts (10–15 µg) were subjected to SDS–polyacrylamide gel electrophoresis, transferred to PVDF membranes and blocked with I-Block (ThermoFisher, T2015). To detect frataxin, nitrocellulose membranes were used and blocked with I-Block. Primary antibodies used were: frataxin (1:1000 Abcam, ref. Ab219414), OxPhos (1:20,000 Invitrogen, ref. 458,099 to detect CII, III, IV and V, and 1:1,000 to detect CI), SOD2 (1:2,000 AbCam, ref. Ab13533), acetylated Lys68 SOD2 (1:2,000 AbCam, ref. Ab137037), Tubulin (1:50,000 Sigma, ref. T5168), acetylated Lys40 alpha tubulin (1:20,000 Proteintech, ref. 66,200), SirT2 (1:3,000 Santa Cruz, ref. Sc28298), SirT3 (1:2,000 Proteintech, ref. 10,099-1AP to detect mouse SirT3), SirT3 (1:1,000 Invitrogen, ref. MAB14910 to detect rat SirT3), MEC17 (1:500 Sigma, ref SAB2109036), 4-Hydroxynonenal (HNE)-Michael adducts (1:2,000 Calbiochem, ref. 393,207) and acetylated-lysine (1:2,000 Cell Signaling, ref. CST9681S). After blotting, PVDF membranes were stained with Coomassie brilliant blue (CBB) and nitrocellulose membranes with Colloidal Gold (Bio-Rad). Total protein stain was quantified with the Image Lab software (Bio-Rad) and used as loading control for normalization of target proteins.

Electron and optical microscopy images

WT and FXN^{151F} mice were perfused with 1% PFA and 1% glutaraldehyde in 0.1 M PB (pH 7.4) for conventional electron microscopy. Pieces DRGs were dissected, post-fixed in 1% osmium tetroxide for 2 h and then contrasted with 0.5% uranyl acetate for 30 min; all procedures were conducted at 4 ℃. Samples were processed for Embed 812 (Electron Microscopy Sciences, Hatfield, PA, USA) embedding according to standard procedures. Ultrathin Sects. (80–90 nm thick) were counterstained with uranyl acetate and lead citrate and observed in a Tecnai Spirit electron microscope (Unitat de Criomicroscòpia Electrònica, Universitat de Barcelona). For mitochondrial area measurements, images were analyzed using Image J software.

Semithin Sects. (0.5 µm thick) were made using a Leica ultramicrotome (Leica EM UC6, Wetzlar, Germany) and mounted onto glass slides. Mounted sections were then dried on a hot plate. Richardson stain (which contains methylene blue, azur II and sodium tetraborate) was performed according to standard protocols. Images were captured in a Olympus BX50 microscope.

NAD^+ and NADH measurement

NAD^+ and NADH measurement in DRG tissue or cell cultures was carried out using the EnzyChromTM NAD^+/NADH Assay Kit (E2ND-100) according to the manufacturer's protocol. In brief, DRG tissue or cell cultures were homogenized with 100 µL of NAD^+ or NADH extraction buffer. Extracts were heated for 5 min at 60ºC and 20 µL of the assay buffer was added, followed by 100 µL of the opposite buffer extraction (to neutralize the extracts). Mixtures were centrifuged at 14,000 rpm for 5 min and 40 µL of the supernatant were transferred into a 96-well plate and assayed as indicated. Optical density at 565 nm was recorded at time zero, and after 30 min, using a 96-well plate reader spectrophotometer. A standard curve was performed to determine the NAD^+/NADH concentration of the samples.

Sirtuin activity

Total sirtuin activity was measured using a SirT3 activity assay kit (Abcam, ab156067) in line with the manufacturer's protocol. DRGs or cultured cells were resuspended in PBS, sonicated, and centrifuged at 14,000 rpm for 5 min. Trichostatin A, which selectively inhibits the class I and II mammalian histone deacetylases, but not class III (sirtuins) was added to give a final concentration of 5 µM. The fluorescence intensity was measured for 30 min at 5 min intervals on a fluorometric microplate reader (Tecan infinity M200 pro) with excitation at 340–360 nm and emission at 440–460 nm. Data were normalized by protein concentration. Sirtuin activity was represented as relative levels of fluorescence intensity.

Two-dimensional (2D) electrophoresis

Isolated DRGs from mice were disrupted under liquid nitrogen using a mortar and pestle, and ground to a fine powder. The powder was resuspended in rehydration buffer containing 7 M urea, 2 M thiourea, 4% Chaps, 50 mM dithiothreitol (DTT) plus protease inhibitors (Roche). After incubation (30 min in a shaker at 25 ℃), 0.5% (v/v) ampholytes, pH 3–10 (GE Healthcare Life Sciences), and bromophenol blue were added and centrifuged (14,000 rpm for 10 min) to remove insolubilized material. Isoelectric focusing was performed in immobilized pH gradient strips (17 cm, pH 3–10 NL; Bio-Rad). The focused strips were stored at − 80 ℃ until second-dimension electrophoresis was performed. Thawed strips were equilibrated for 15 min in 370 mM Tris–HCl pH 8.8 containing 6 M urea, 2% (w/v) SDS, 20% (v/v) glycerol, and 130 mM DTT and then reequilibrated for 15 min in the same buffer containing 135 mM iodoacetamide in place of DTT. Second-dimension SDS-PAGE was performed on 11% polyacrylamide gels. Gels were stained with the fluorophore Oriole (Rio-Rad) or transferred to PVDF for western blot anti acetyl-Lys. In both cases, images were scanned with a Chemidoc CCD camera (Bio-Rad) and analyzed with PDQuest software (Bio-Rad). Acetylated protein was excised from the Oriole stained gel, and identified after in-gel trypsin digestion followed by mass spectrometry at the Mass Spectrometry and Proteomics Core Facility of the Institut de Recerca Biomèdica de Barcelona (IRBB).

Mitochondrial superoxide and mitochondrial iron

Mitochondrial superoxide content was detected with the MitoSOX Red probe (ThermoFisher, M36008), and mitochondrial Fe^{2+} content was determined with the Mito-FerroGreen probe (Dojindo, M489-10) according to the manufacturer's instructions. In both cases, DRG neurons were placed in ibiTreat 4-well m-slides (Ibidi, Cat#80,286) pretreated with 0.1 mg/mL of collagen. Three or four days after lentivirus transduction, cells were washed three times with warm buffer (Hank's buffered saline solution and 10 mM HEPES medium) and incubated for 10 min with 5 µM MitoSox probe (λex: 510 nm; λem: 580 nm), or for 30 min with 5 µM Mito-FerroGreen probe (λex:488 nm; λem: 500 nm) diluted in Hank's buffered saline solution medium. Cells were washed three times and images recorded by confocal microscopy (Olympus FV1000) with a 100 × objective using the Z stack configuration. All the images were acquired with the same laser intensity (respect to the Scr), image bit-depth: 12 bits, image resolution: 1024 × 1024 pixels, scan mode: XYZ, scan direction: one-way and sequential mode: frame.

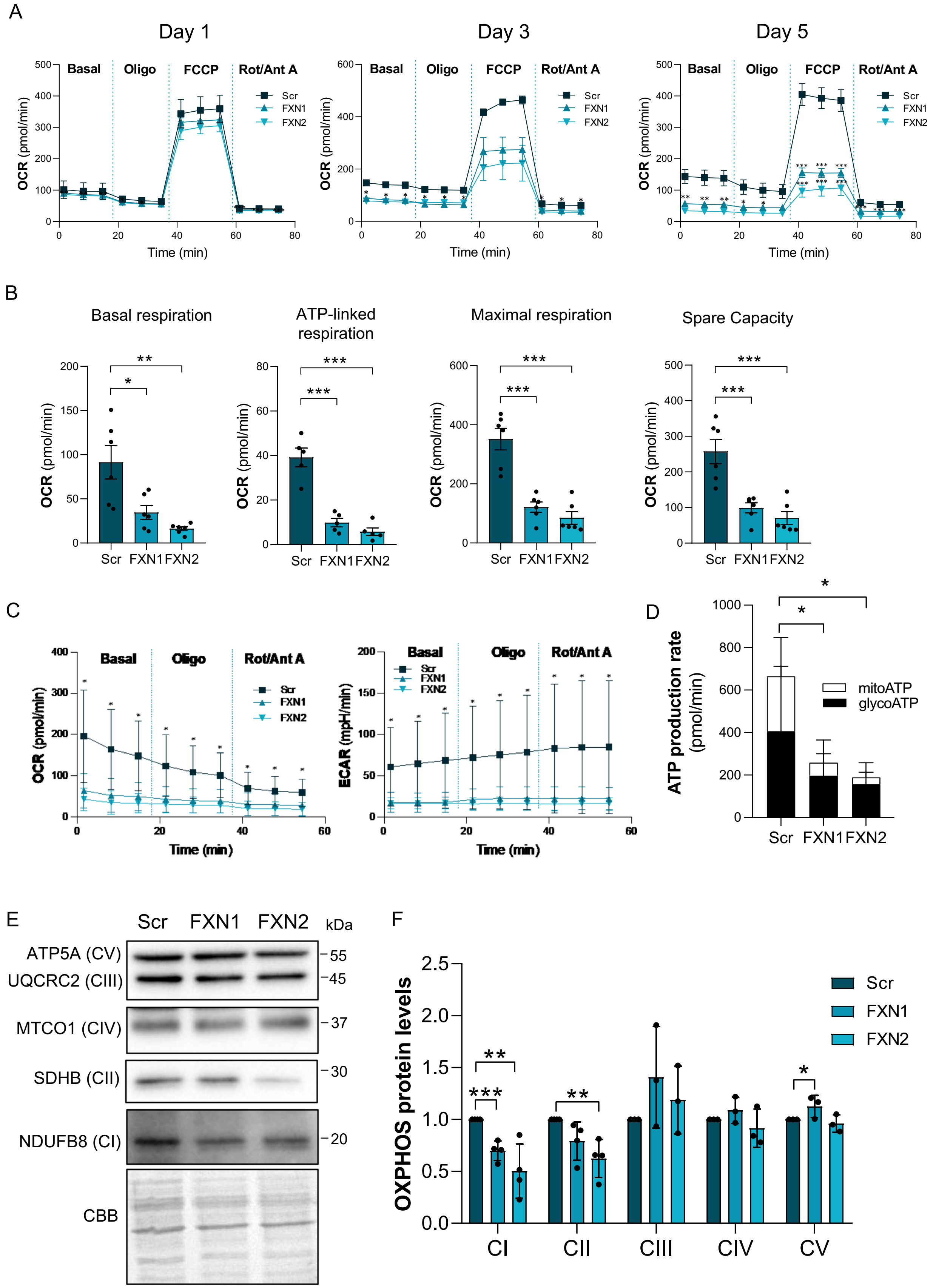
A
Day 1
Day 3
Day 5
Basal
Oligo
FCCP
Rot/Ant A
Scr
FXN1
FXN2
OCR (pmol/min)
Time (min)
B
Basal respiration
ATP-linked respiration
Maximal respiration
Spare Capacity
OCR (pmol/min)
Scr FXN1 FXN2
C
Basal
Oligo
Rot/Ant A
OCR (pmol/min)
ECAR (mpH/min)
Time (min)
D
ATP production rate (pmol/min)
mitoATP
glycoATP
Scr FXN1 FXN2
E
Scr FXN1 FXN2
kDa
ATP5A (CV)
UQCRC2 (CIII)
MTCO1 (CIV)
SDHB (CII)
NDUFB8 (CI)
CBB
55
45
37
30
20
F
OXPHOS protein levels
CI
CII
CIII
CIV
CV

◂**Fig. 1** Mitochondrial ETC complexes are impaired in primary cultures of frataxin-deficient DRG neurons. **A** Mitochondrial stress analysis of frataxin-deficient DRG neurons (FXN1 and FXN2) compared to control cells (Scr) at day 1, 3 and 5 after lentivirus transduction (OCR: Oxygen consumption rate) (n = 2 independent cultures at day 1 and 3; n = 6 independent cultures at day 5). **B** Basal respiration, ATP production, maximal respiration rate, and spare capacity of FXN1 and FXN2 neurons compared to Scr at day 5 after lentivirus transduction (n = 6 independent cultures). **C** OCR and extracellular acidification rate (ECAR) of FXN1 and FXN2 cells compared to control Scr cells at day 5 after lentivirus transduction (n = 4 independent cultures). **D** Mitochondrial and glycolytic ATP production rates were obtained from **C**. **E** Indicated proteins of the mitochondrial OXPHOS system were analyzed by western blot in Scr, FXN1 and FXN2 primary culture homogenates (at day 5 after lentivirus transduction). Representative western blot images are shown. **F** Histograms represent the mean ± SD from n = 3–4 independent experiments. CBB protein stain was used as a loading control. Data are the mean ± SD. Unpaired t test was performed (**B**, **D**, **C** and **F**). Significant differences between Scr and FXN1 or FXN2 are indicated (p values < 0.05(*), 0.01(**), or 0.001(***))

Mitochondrial fluorescence intensity per cellular soma was quantified using Image J analysis software.

Statistical analysis

Data are presented as means ± SD. Statistical analysis were performed as specified in each figure legend. P-values lower than 0.05 (*), 0.01 (**) or 0.005 (***) were considered significant. GraphPad Prism 5.0 was used for all graphs. For primary cultures of DRG neurons, the data were obtained from at least three independent isolations (referred to as n number). For each isolation, an average of 15 rats were used. In isolated DRGs from mice, the number of animals used in each study (n number) is listed in the figure legend.

Results

Mitochondrial impairment in primary cultures of frataxin-deficient DRG neurons

Several reports have demonstrated that mitochondrial respiration is impaired in different tissues as a consequence of decreased frataxin levels. Among them, heart has been the most studied [34, 35], but it has also been demonstrated in other FA models, like skin fibroblasts, lymphoblasts, and lymphocytes [36, 37]. However, how frataxin affects sensory neurons, the primary target in FA, has remained unresolved [38]. In this study, to determine whether mitochondrial respiration was also affected in DRG neurons, they were isolated from neonatal rats and transduced with lentiviral vectors carrying frataxin-interfering shRNA (FXN1 or FXN2) or a non-interfering shRNA (Scr) as a control. Using this model, as previously shown [11], frataxin levels began to decline as early as 24 h after transduction; this decline continued for 5 days with frataxin-targeting shRNAs (Supplementary Fig. 2A and B). At the end of the experiment, 5 days after transduction, frataxin levels were reduced to 20–30%, the mean values for shRNAs FXN1 and FXN2 respectively, which were similar to those values found in FA patients. Cell viability also decreased progressively from day 1 to day 5, being 55% and 40% in FXN1 and FXN2 cultures, respectively, at day 5 (Supplementary Fig. 2C). The Seahorse technology allowed us to determine the time course effect of decreased frataxin levels on mitochondrial respiration in primary cultures of DRG neurons. The oxygen consumption rate (OCR) was measured the following conditions: basal respiration, oligomycin addition (a complex V inhibitor), FCCP addition (an uncoupling agent) and rotenone/antimycin A addition (rotenone inhibits complex I and antimycin A inhibits complex III). As shown in Fig. 1A, the decrease in OCR was correlated with frataxin decay. Using these data, several parameters were quantified 5 days after transduction (Fig. 1B). Basal respiration, ATP-linked respiration, maximal respiration and spare capacity, all decreased following transduction with shRNAs FXN1 and FXN2 compared to non-interfering shRNA (Scr). In addition, the mitochondrial ATP production rate (mitoATP) versus cytosolic ATP production rate (GlycoATP) was determined by combining OCR data with extracellular acidification rate (ECAR) (Fig. 1C). As shown in Fig. 1D, FXN1 and FXN2 cells displayed a huge reduction (80–85%) in mitoATP production rate compared to Scr cells. These results are consistent with previous results from our group demonstrating that frataxin reduction induced mitochondrial depolarization in primary cultures of DRG neurons [31].

Since frataxin is involved in Fe-S cluster synthesis, it is possible that such deficiencies in activity are due to decreased protein levels, as several proteins in electron transport chain (ETC) complexes contain Fe-S. To this end, mitochondrial ETC complexes were analyzed by western blot from primary cultures of DRG neurons (Fig. 1E). Cell extracts of FXN2 cultures displayed around a 50% reduction in SDHB (complex II) and NDUFB8 (complex I) protein levels compared to Scr cultures (Fig. 1F). Nevertheless, no differences in UQCRC2 (complex III), MTCO1 (complex IV) or ATP5A (complex V) were found between FXN1 or FXN2 and Scr cultures (Fig. 1F).

Functional and morphological alterations in mitochondrial DRGs from FXN^{I151F} mouse model

To analyze whether such differences also occur in vivo, we used the new mouse model FXN^{I151F} carrying a missense point mutation equivalent to human I154F [29]. In homozygosity, these mice present low levels of frataxin in all tissues and start to show neurological symptoms at 23 weeks of age.

It is known that they present mitochondrial alterations that are more marked in the nervous system (cerebrum and cerebellum) than in the heart, but DRG neurons have not been analyzed previously [29].

Here, we isolated DRGs from 21- and 39-week-old WT and FXN^{I151F} mice. Frataxin levels in the mutant mice were 3–8% compared to WT mice both at 21 and 39 weeks old (Fig. 2A and B). To study mitochondrial function, the enzymatic activity of mitochondrial ETC complexes was determined. As shown in Fig. 2C, at 21 weeks of age, DRG homogenates from FXN^{I151F} mice showed no differences in complex I + III activity compared to WT mice. However, differences were statistically significant at 39 weeks. Interestingly, complex II + III activity showed a significant reduction in FXN^{1515F} mice compared to WT at 21 weeks, as well as at 39 weeks (Fig. 2D). Citrate synthase has usually been used as an indication of mitochondrial content. Thus, we measured citrate synthase activity, and no differences were observed (Supplementary Fig. 3). Next, the levels of several proteins from the mitochondrial ETC from DRG homogenates from 21- and 39-week-old WT and FXN^{I151F} mice were analyzed (Fig. 3A). At 21 weeks of age, only mitochondrial SDHB from complex II showed significant differences (Fig. 3B). At 39 weeks of age, there was a decrease in NDUB8 from complex I and in SDHB from complex II. At both ages, no differences were found in UQCRC2 (complex III), MTCO1 (complex IV) or ATP5A (complex V) in FXN^{151F} versus WT animals (Fig. 3B).

The neurological phenotype observed in FA patients reflects lesions in DRGs, sensory peripheral nerves, corticospinal tracts, and dentate nuclei, which have been described at histological level [8]. Accordingly, we further analyzed whether the functional alterations we observed in the mitochondria from the FXN^{I151F} mice may have a morphological consequence. Electron microscopy images revealed, in a small percentage of cells, two main types of mitochondrial defects in the mutant mice at 39 weeks of age: abnormal mitochondria without cristae, and condensed mitochondria (Fig. 3C and D). The presence of abnormal mitochondria without cristae was also detected on semithin sections stained with methylene blue (Supplementary Fig. 4). In addition, we analyzed the size of mitochondria from DRG micrographs and, as shown in Fig. 3E, mitochondrial area was increased in FXN^{I151F} mice compared to WT mice.

Reduced NAD$^+$/NADH ratio and decreased sirtuin activity in FXN-deficient DRGs

The results described above showed that deficiency of frataxin induced an impairment in the mitochondrial ETC, mainly affecting complex I and II. These alterations might lead, in addition to an ATP deficiency (Fig. 1D), to other consequences such as alterations in the NAD$^+$/NADH ratio. As shown in Fig. 4A, this ratio was highly reduced (fivefold) in frataxin-deficient primary cultures of DRG neurons (FXN1) compared to control cultures (Scr). Although differences were not as great, a decreased NAD$^+$/NADH ratio was also found in DRG homogenates from 21-week-old mutant mice compared to WT mice. At 39 weeks of age, the NAD$^+$/NADH ratio showed a tendency to decrease in mutant mice compared to WT mice, but no statistically significant differences were found (Fig. 4B).

It has previously been reported that increased NAD$^+$ levels in a FA cardiomyopathy model improved cardiac function in a SirT3-dependent manner [39]. In mitochondria, SirT3 is the main NAD$^+$-dependent deacetylase, and SirT3 inhibition and protein hyperacetylation have a negative feedback effect contributing to cardiomyopathy in FA [25, 40]. Although the role of SirT3 in FA cardiomyopathy is known and several acetylated proteins have been described [40], there is no information on how NAD$^+$ reduction may affect protein acetylation in sensory neurons. Since it was impractical to analyze only SirT3 activity in our primary cultures, total sirtuin activity was measured, with SirT1, SirT2 and SirT3 being the sirtuins with the highest deacetylase activity [20]. The results showed a 35–40% decrease in sirtuin activity in FXN1 cells compared to Scr (Fig. 4C). Total sirtuin activity was also analyzed in DRG homogenates from FXN^{I151F} and WT mice. As shown in Fig. 4D, a 40% (21-week-old) and 30% (39-week-old) reduction was detected in the mutant mice compared to WT mice.

Increased protein acetylation in FXN-deficient DRGs

A reduction in sirtuin activity would be expected to lead to an increase in protein acetylation. To that end, western blots anti acetyl-Lys were performed using DRG homogenates from WT and mutant mice at 21 and 39 weeks of age. A highly prominent acetylated band of 52 kDa appeared in all samples (Fig. 5A). At 21 weeks, this band presented no significant differences in acetylation in the mutant mice compared to WT animals. However, at 39 weeks, the differences in protein acetylation between WT and mutant mice increased by up to 2.5-fold (Fig. 5B). We identified this protein as alpha tubulin using 2-dimensional gel electrophoresis followed by mass spectrometry (Supplementary Fig. 5A and B). Alpha-tubulin is regulated by acetylation, among several other posttranslational modifications. Since specific antibodies for acetylated alpha tubulin at the Lys40 residue were available, western blot was performed (Fig. 5C). Similarly, to that observed with the acetyl-Lys antibody, we corroborated that tubulin acetylation was significantly increased in 39-week-old FXN^{I151F} mice compared to WT mice, once normalized by total tubulin (Fig. 5D and Supplementary Fig. 6). At 21 weeks of age, no differences were detected.

Fig. 2 DRGs from FXN^{I151F} mice present reduced mitochondrial complex I and II activities. **A** Relative mature frataxin (15 kDa) content analyzed by western blot in DRG homogenates from 21- and 39-week-old WT and FXN^{I151F} mice. Representative images from frataxin western blot membranes under nonsaturating conditions are shown. **B** Data represent the mean ± SD from n = 6 different mice. Unpaired t test was performed. Colloidal gold protein stain was used as a loading control. **C** Complex I + III, and **D** complex II + III activities were measured in DRG homogenates from 21- and 39-week-old WT and FXN^{I151F} mice. Data are the mean ± SD from n = 4–5 animals/group. Each biological replicate is color-coded (day to day variability), and small symbols represent experimental replicates. Paired t test was used (**C** and **D**), except for CI + III (39w) were a Wilcoxon matched-pairs signed rank test was performed. Significant differences between WT and FXN.^{I151F} mice are indicated (p values < 0.05(*), 0.01(**) or 0.001(***))

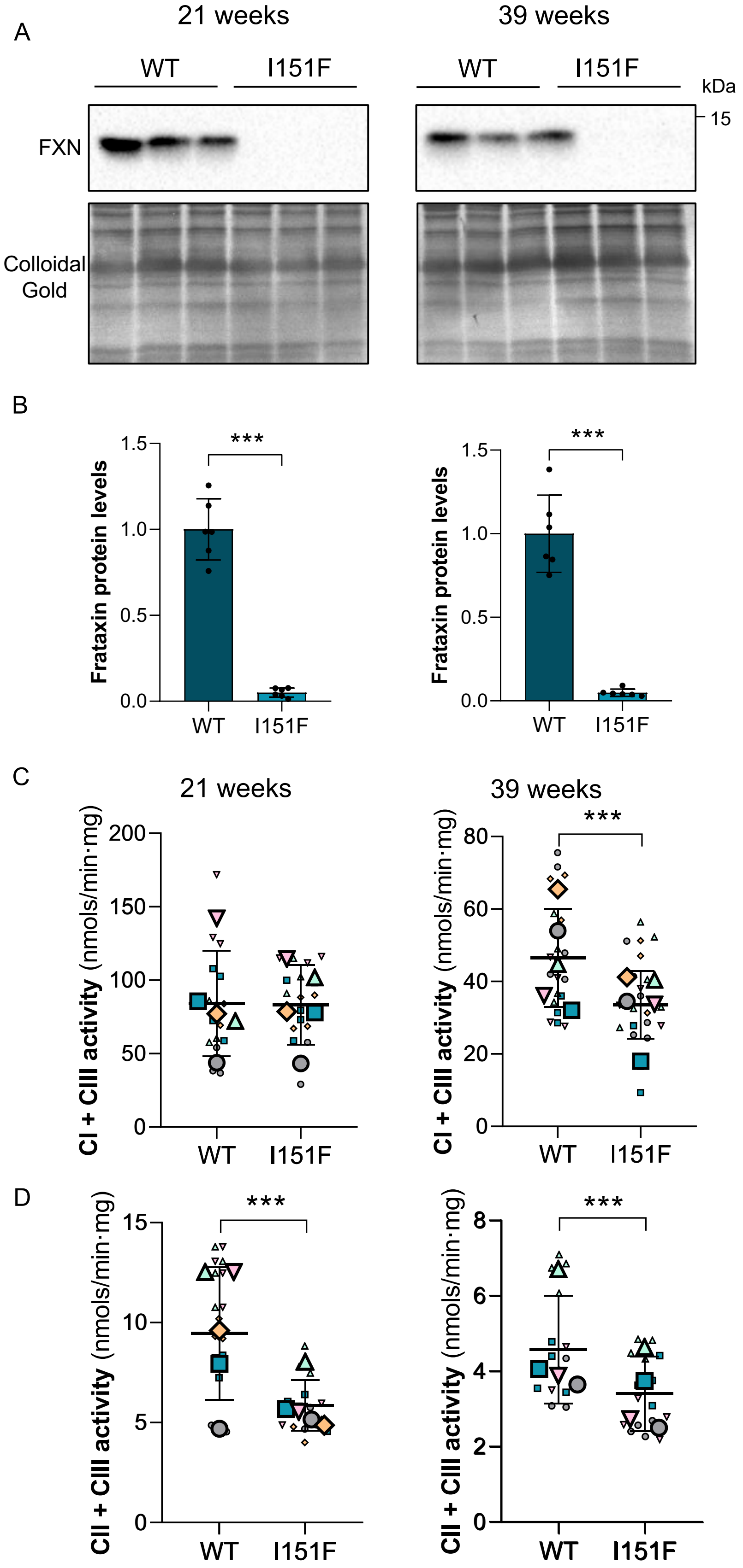

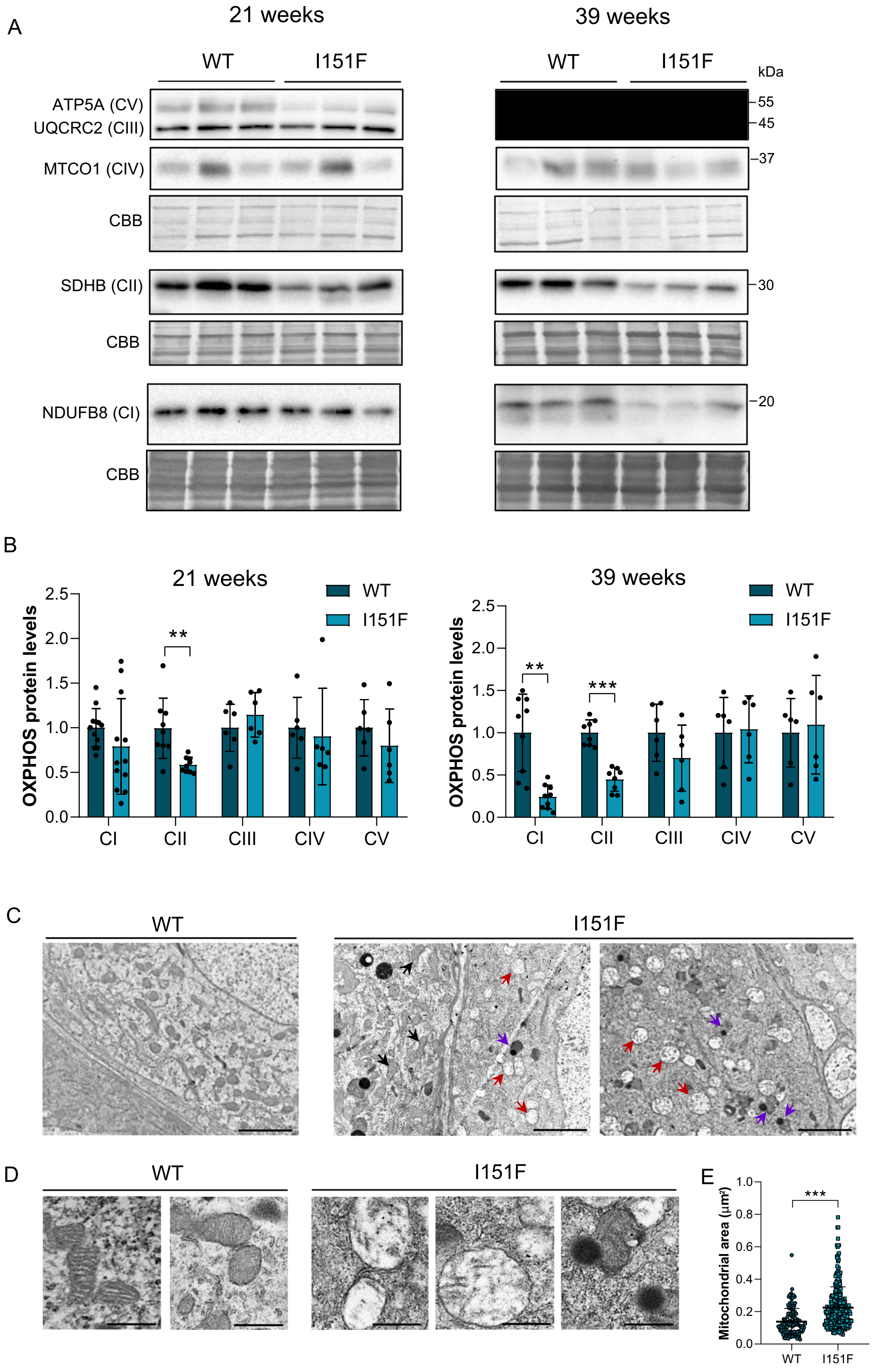
A
21 weeks
39 weeks
WT
I151F
WT
I151F
kDa
ATP5A (CV)
UQCRC2 (CIII)
MTCO1 (CIV)
CBB
SDHB (CII)
CBB
NDUFB8 (CI)
CBB
55
45
37
30
20
B
21 weeks
39 weeks
WT
I151F
OXPHOS protein levels
2.5
2.0
1.5
1.0
0.5
0.0
**
***
CI
CII
CIII
CIV
CV
C
WT
I151F
D
WT
I151F
E
Mitochondrial area (µm²)
1.0
0.8
0.6
0.4
0.2
0.0
***
WT
I151F

◂**Fig. 3** DRGs from FXN^{I151F} mice showed reduced mitochondrial complex I and II and mitochondrial degeneration. Indicated proteins of the mitochondrial OXPHOS system were analyzed by western blot of DRG homogenates from 21- and 39-week-old WT and FXN^{I151F} mice. **A** Western blot images are shown. **B** Histograms represent the mean ± SD from n = 6–12 animals/group. CBB protein stain was used as a loading control. Unpaired t test was performed. **C** Electron micrographs of DRGs from WT and FXN^{151F} mice at 39 weeks. Neurons with apparent normal mitochondria (black arrows) together with mitochondria with abnormal mitochondria without cristae (red arrows) and condensed mitochondria (violet arrows) were detected in the mutant mice. Scale bar: 2 µm. **D** Higher magnification of electron micrographs showing mitochondria ultrastructure: normal mitochondria (WT mouse), and both mitochondria without cristae and condensed mitochondria (FXN^{151F} mouse). Scale bar: 500 nm. **E** Quantification of mitochondrial area of DRGs from WT and FXN^{151F} mice. Data are from multiples images from 3 different mice per group. Between 130 (WT) and 280 (I151F) mitochondria were analyzed. Mann–Whitney test was conducted. Significant differences between WT and FXN.^{I151F} mice are indicated (p values < 0.05(*), 0.01(**), or 0.001(***))

Tubulin acetylation is the result of the activity of deacetylases and acetyl transferases. SirT2 and HDAC6 are the main tubulin deacetylases [41]. We determined levels of SirT2 in DRG homogenates from 21- and 39-week-old FXN^{I151F} mice (Fig. 5E), and a significant decrease was found at 39 weeks, compared to their controls (Fig. 5F). On the other hand, MEC17 (also known as Atat1) is the major tubulin acetyltransferase in mice [42] and it was reported to be increased in a cellular model of FA [43]. To determine whether this also occurs in the DRGs from FXN^{I151F} mice, we measured MEC17 levels at 21 and 39 weeks of age. As shown in Fig. 5G and D, a 1.8-fold (21-week-old) and 2.9-fold (39-week-old) increase was detected in the mutant mice compared to WT mice.

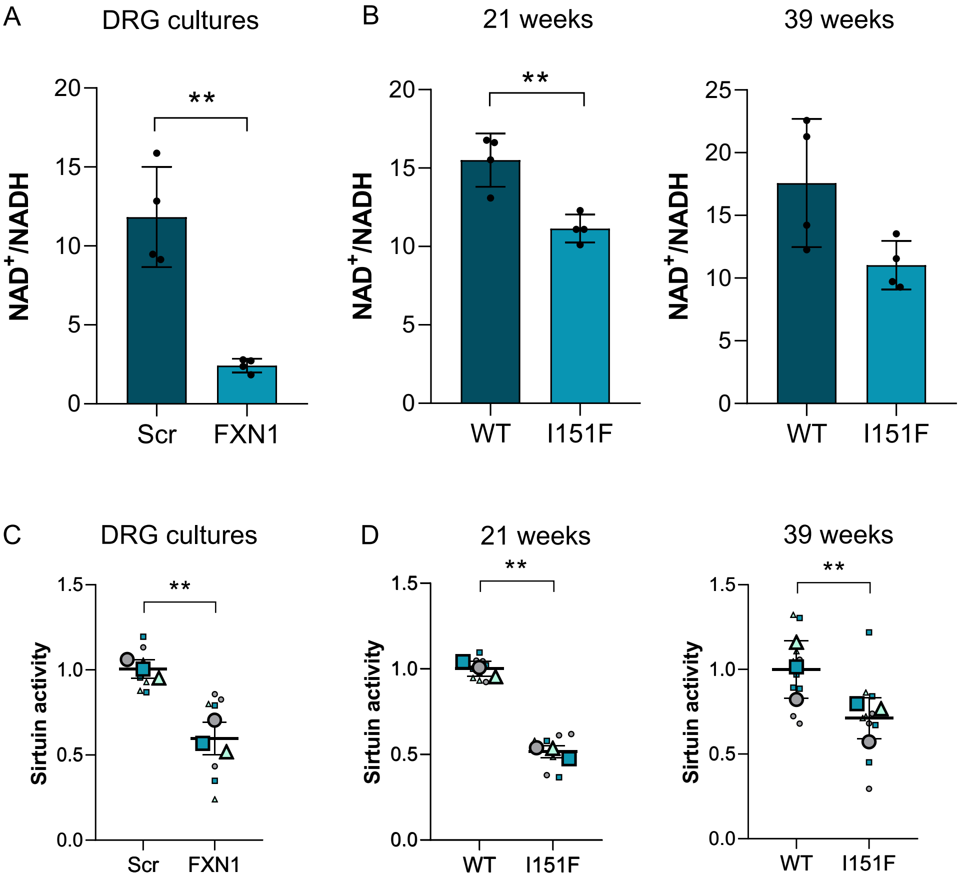

Fig. 4 Reduced levels of NAD$^+$/NADH ratio and sirtuin activity in primary cultures of DRG neurons and DRGs from FXN^{I151F} mice. **A** NAD$^+$/NADH ratio was measured in frataxin-deficient DRG neurons (FXN1) compared to control cells (Scr) at day 5 after lentivirus transduction (n = 4 independent cultures). **B** NAD$^+$/NADH ratio measured in DRG homogenates from 21- and 39-week-old FXN^{I151F} mice and compared to WT mice (n = 4 mice/group). Unpaired t test was performed (**A** and **B**). **C** Total sirtuin activity in DRG homogenates from frataxin-deficient DRG neurons (FXN1) compared to control cells (Scr) was measured at day 5 after lentivirus transduction. Trichostatin A was added to the assay to inhibit NAD-independent histone deacetylases. Quantification data are mean ± SD obtained from n = 3 independent isolations. **D** Total sirtuin activity was measured in DRG homogenates from 21- and 39-week-old FXN.^{I151F} mice and compared to WT mice. Quantification data are mean ± SD obtained from n = 3 mice/group. In **C** and **D**, each biological replicate is color-coded (day to day variability), and small symbols represent experimental replicates. Data represent the mean ± SD. Paired t test was performed (**C** and **D**). Significant differences are indicated (p values < 0.05(*), 0.01(**), or 0.001(***))

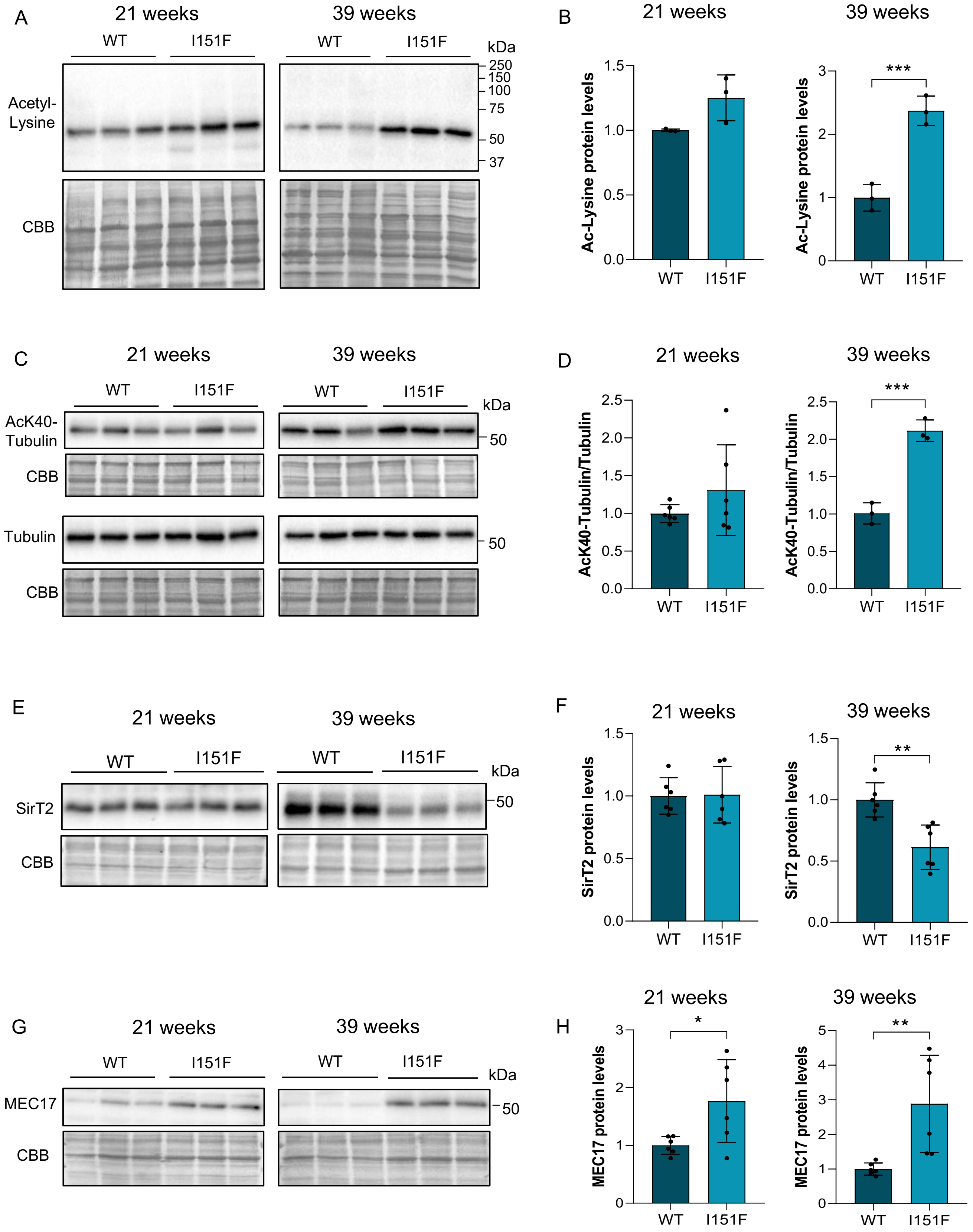
A
21 weeks
39 weeks
WT
I151F
WT
I151F
kDa
250
150
100
75
50
37
Acetyl-Lysine
CBB
B
21 weeks
39 weeks
Ac-Lysine protein levels
1.5
1.0
0.5
0.0
3
2
1
0
***
WT
I151F
WT
I151F
C
21 weeks
39 weeks
WT
I151F
WT
I151F
kDa
AcK40-Tubulin
CBB
Tubulin
CBB
50
50
D
21 weeks
39 weeks
AcK40-Tubulin/Tubulin
2.5
2.0
1.5
1.0
0.5
0.0
***
WT
I151F
WT
I151F
E
21 weeks
39 weeks
WT
I151F
WT
I151F
kDa
SirT2
CBB
50
F
21 weeks
39 weeks
SirT2 protein levels
1.5
1.0
0.5
0.0
**
WT
I151F
WT
I151F
G
21 weeks
39 weeks
WT
I151F
WT
I151F
kDa
MEC17
CBB
50
H
21 weeks
39 weeks
MEC17 protein levels
3
2
1
0
5
4
3
2
1
0
*
**
WT
I151F
WT
I151F

◂ **Fig. 5** Identification and analysis of alpha tubulin as a highly acetylated protein. **A** Western blot analysis of acetylated proteins from DRG homogenates from 21- and 39-week-old WT and FXN^{I151F} mice. **B** Quantification data of A are mean ± SD obtained from n = 3 mice/group. CBB protein stain was used as a loading control. **C** Alpha-tubulin acetylated at Lys40 and total tubulin were analyzed by western blot from DRG homogenates from 21- and 39-week-old WT and FXN^{I151F} mice. **D** Histogram data from C are represented as means ± SD from n = 3–6 mice/group. CBB protein stain was used as a loading control. **E** SirT2 protein levels were analyzed in DRG homogenates from 21- and 39-week-old FXN^{I151F} mice and compared to WT mice. **F** Quantification data of E are mean ± SD obtained from n = 6 mice/group. CBB protein stain was used as a loading control. **E** MEC17 was analyzed by western blot from DRG homogenates from 21- and 39-week-old WT and FXN.^{I151F} mice. **F** Histogram data from E are represented as means ± SD from n = 6 mice/group. CBB protein stain was used as a loading control. Unpaired t test was performed (**B**, **D**, **F**, and **H**). Significant differences are indicated (p values < 0.05(*), 0.01(**), or 0.001(***))

SOD2 acetylation and oxidative stress increase in frataxin-deficient DRGs

Since frataxin is a mitochondrial protein and we were especially interested in mitochondria, we also determined levels of mitochondrial SirT3 in DRG homogenates from 21- and 39-week-old FXN^{I151F} mice. Decreased SirT3 levels were found at 21 weeks compared to their controls (Fig. 6A and B), but no significant differences were found at 39 weeks. A well-known target of SirT3 is mitochondrial SOD2. To understand how decreased sirtuin activity and SirT3 levels may affect it, acetylated SOD2 and total SOD2 were analyzed in 21- and 39-week-old FXN^{I151F} and WT mice (Fig. 6C). As shown in Fig. 6D, the results demonstrated increased acetylation at both ages (21 and 39 weeks) in the mutant mice. Intriguingly, at 21 weeks, the difference in SOD2 acetylation between mutant and WT mice was much higher than at 39 weeks, once normalized by total SOD2 levels (Fig. 6D and Supplementary Fig. 7). It is well known that acetylation at Lys68 inactivates SOD2 [44], and we hypothesize that this might result in oxidative stress. To that end, hydroxynonenal (HNE), a well-studied oxidative stress marker, was analyzed (Fig. 6E). HNE is an α,β-unsaturated hydroxyalkenal generated as a byproduct of lipid peroxidation that can be detected and quantified by western blot, because it covalently binds to specific proteins. As shown in Fig. 6F, HNE was increased in DRG homogenates from FXN^{I151F} mice both at 21 and 39 weeks of age compared to WT mice.

To study whether such oxidative stress could also be observed in primary cultures of DRG neurons, we analyzed SirT3 levels and SOD2 acetylation in Scr, FXN1 and FXN2 cultures. Western blotting revealed a significant decrease in SirT3 levels in FXN1 and FXN2 cells compared to Scr cells (Fig. 7A and B). The results also showed that FXN1 and FXN2 cells presented a 2- to threefold increase in SOD2 acetyl-Lys68 levels compared to Scr, once normalized by total SOD2 levels (Fig. 7C and D and Supplementary Fig. 8). To study the effect of increased SOD2 acetylation on frataxin-deficient DRG neurons, the fluorescent dye MitoSox Red was used. First, to ascertain the main mitochondrial localization of this probe, we performed a dual labelling of DRG neurons with MitoTracker Green (Fig. 7E). Afterwards, superoxide levels were analyzed in Scr, FXN1 and FXN2 cultures (Fig. 7F). As shown in Fig. 7G, FXN1 and FXN2 cultures with reduced frataxin levels showed increased mitochondrial superoxide levels compared to Scr cells.

Another trait that can cause oxidative stress is iron accumulation, especially ferrous iron (Fe^{2+}). Published evidence indicates that frataxin deficiency causes an imbalance in iron homeostasis. Iron deposits or accumulation have been observed in frataxin-deficient models [45], but their role in the progression of the disease remains unclear [46]. To analyze whether iron accumulates in sensory neurons of DRG, the fluorescent probe Mito-FerroGreen was used. This compound enables live cell fluorescent imaging of intramitochondrial Fe^{2+}. Again, to test mitochondrial localization, dual labelling was performed with the mitochondrial probe MitoTracker Red (Fig. 7H). Labelling with Mito-FerroGreen and the quantification of fluorescence in the soma of DRG neurons showed an approximately 1.5–twofold iron accumulation in FXN1 and FXN2 cells compared to Scr cells (Fig. 7I and J). In summary, all these changes contribute to oxidative stress that affects the whole cell but in particular the mitochondria in the sensory neurons.

Honokiol alleviates mitochondrial dysfunction

To better understand the role of SirT3 in the mitochondrial deterioration observed in frataxin-deficient cells, Scr, FXN1 and FXN2 primary cultures were treated with honokiol, a well-known SirT3 activator [27]. As shown in Fig. 8A, honokiol treatment reduced the decay in oxygen consumption observed in FXN1 and FXN2 compared to Scr cells. Honokiol increased basal respiration by 30%, 58% and 98% in Scr, FXN1 and FXN2 cells, respectively. Maximal respiration was increased by 18%, 52% and 89% in Scr, FXN1 and FXN2 cells, respectively. The recovery observed was significant under all conditions analyzed, but it was higher in FXN1 and FXN2 than in Scr cultures (Fig. 8B-D). To ascertain whether such an effect is due to increased SirT3 activity, we measured the acetylation of mitochondrial SOD2 upon honokiol treatment. As shown in Fig. 8E, honokiol-treated FXN1 and FXN2 cells resulted in a reduction of SOD2 acetylation, reaching similar levels to those in Scr cells. The recovery was significant for both FNX1 and FXN2 (Fig. 8F and Supplementary Fig. 9). Since the deacetylation of SOD2 increases its catalytic activity, we measured mitochondrial

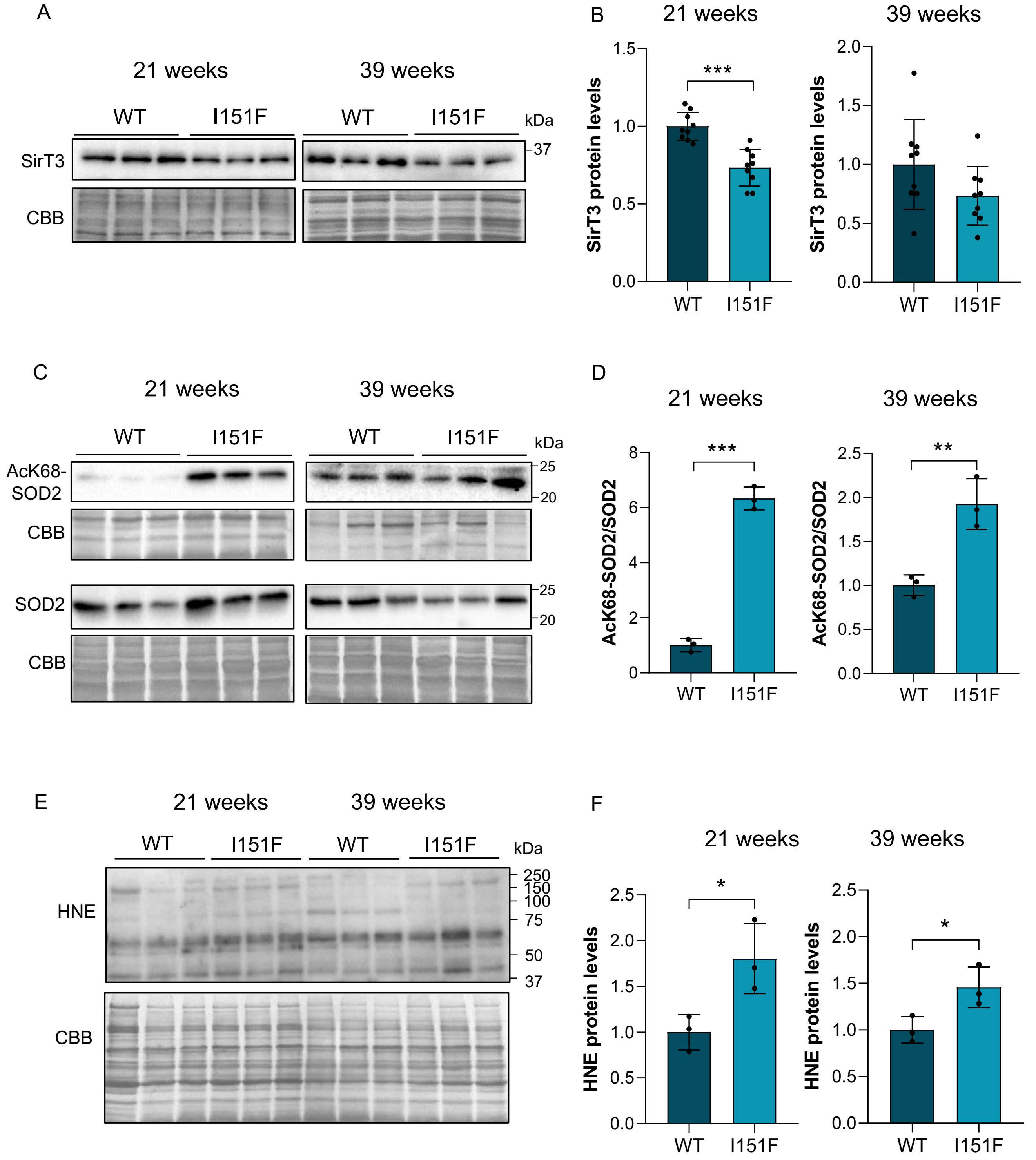

Fig. 6 Increased acetylated SOD2 and HNE levels in the mutant mice. **A** SirT3 protein levels were analyzed in DRG homogenates from 21- and 39-week-old FXN^{I151F} mice and compared to WT mice. **B** Quantification data of A are mean ± SD obtained from n = 9 mice/group. CBB protein stain was used as a loading control. **C** SOD2 acetylated at Lys68 and total SOD2 were analyzed by western blot of DRG homogenates from 21- and 39-week-old WT and FXN.^{I151F} mice. **D** Histograms represent the mean ± SD from n = 3 mice/group. CBB protein stain was used as a loading control. **E** HNE bound to proteins was analyzed by western blot from DRG homogenates of 21- and 39-week-old mice. **F** Histograms represent the mean ± SD from n = 3 mice/group. CBB stain was used as a loading control. Unpaired t test was performed (**B**, **D**, and **F**). Significant differences between WT and mutant animals are indicated (p values < 0.05(*), 0.01(**), or 0.001(***))

superoxide levels with the MitoSox Red probe in Scr, FXN1 and FXN2 cells treated with honokiol and compared to vehicle-treated cells (Fig. 8G). The quantification of MitoSox Red fluorescence showed an approximately 40% decrease in superoxide levels in both FXN1 and FXN2 cells treated with honokiol compared to cells treated with vehicle (Fig. 8H).

Discussion

Degeneration of DRG large sensory neurons is one of the initial events in FA. However, the effect of frataxin deficiency on their mitochondrial metabolism has not been properly studied [38]. In the present study, we demonstrate that mitochondrial metabolism is impaired in both primary cultures of frataxin-deficient DRG neurons and DRGs from the FXN^{I151F} mouse. In the primary culture model, decreasing levels of frataxin correlated with increasing reductions in oxygen consumption. After 5 days of lentivirus transduction, when frataxin levels were similar to those found in human patients, cells exhibited a strong and consistent decrease in both the OCR (basal and maximal) and total ATP production. As expected, mitochondrial ATP production was strongly impaired but a mild decrease in glycolytic ATP production was also observed. Consequently, mitochondrial membrane potential decreased, as previously described [11].

To determine whether these effects also occur in vivo, we analyzed the consequences of the FXN^{I151F} mutation in mice, which is equivalent to the human I154F pathological mutation. These mice present systemic frataxin deficiency and severe phenotypes, such as decreased weight gain (which is observed from 15 weeks onward), neurological deficits (which start at 23 weeks) and marked biochemical alterations, which become apparent before the appearance of the functional alterations [29]. Based on this information, we conducted our study in mice at 21 weeks of age, before neurologic symptoms appear, and at 39 weeks of age, when the neurological symptoms are clearly apparent. DRGs were isolated from mutant and WT mice and the homogenates were analyzed. Among the complexes of the OXPHOS system, complexes I and II were the most affected. We found a reduction in the content of NDUFB8 (complex I) and SDHB (complex II), consistent with a decline in their enzyme activity. These results are also consistent with the lower levels of complexes I and II observed in the cerebrum, cerebellum, and heart of FXN^{I151F} mice [29]. They also concur with previous results in the KIKO mouse model, where these two complexes showed decreased enzyme activity in cerebella from asymptomatic mice [47]. In the cerebellum, gene expression analysis indicated that this decrease was due to posttranscriptional events [29]. Since NDUF8 and SDHB contain iron-sulfur clusters or belong to complexes containing them, it may be hypothesized that these proteins are degraded due to the absence of cofactor. However, we should be cautious, since FXN^{I151F} mice do not have a general loss of iron-sulfur clusters [29]. Therefore, the mechanism explaining the loss of these proteins may be more complex and could involve different regulatory pathways. It has been reported that astrocyte reactivity contributes to the progression of the disease and that neuron–glia interactions are also important to prevent neurodegeneration in FA [48]. Histological alterations in FA patients have been studied in several tissues of FA patients. One important finding has been the morphological alterations observed in the FXN^{I151F} mice mitochondria, mainly lacking cristae and swollen morphology (Fig. 3C and D). However, it should be noted that only a small percentage of DRG neurons presented mitochondria with such morphological alterations. These results agree with those described in the inducible mouse model of frataxin deficiency model [49], providing evidence for neuronal degeneration of DRGs.

Mitochondrial impairment results in a decreased NAD$^+$/NADH ratio in primary cultures of frataxin-deficient DRG neurons as well as in DRGs from FXN^{I151F} mice. Accordingly, as an NAD$^+$-dependent enzyme, mitochondrial SirT3 activity is expected to decrease in both models. The role of SirT3 in cardiac metabolism has been well described [19], 50. In the context of FA, SirT3 has been studied in two conditional mouse models that develop a fatal cardiomyopathy and impaired activity in respiratory complexes [40]. They showed marked hyperacetylation of cardiac mitochondrial proteins and a huge decrease (85-fold) in the NAD$^+$/NADH ratio. It has also been reported that, using the cardiac/skeletal muscle–specific FXN-KO, activation of SirT3 by nicotinamide mononucleotide supplementation improves both cardiac and extracardiac metabolic function and energy metabolism [19]. In addition, two subunits of complex II, SDHA and SDHB, interacted specifically with SirT3 and were deacetylated and activated by this mitochondrial sirtuin [22].

However, the role of SirT3 in the nervous system and, especially, in sensory neurons has not been studied in FA. In the present study, we observed a fivefold decrease in the NAD$^+$/NADH ratio in FXN1 cell cultures compared to Scr. In FXN^{I151F} mice, the ratio decreased by 30–40% compared to WT animals, a mild reduction compared to results published by Wagner et al. [40] using mitochondria isolated from heart. Such differences may be attributed to the fact that we measured the NAD$^+$/NADH ratio in total DRG homogenates, not mitochondrial preparations. In the present study, the small size of the DRGs did not allow us to purify enough mitochondria to perform this analysis. In addition, DRGs and heart may have different NAD$^+$/NADH ratios, and Wagner et al. used a mouse model that has a complete deficiency of frataxin.

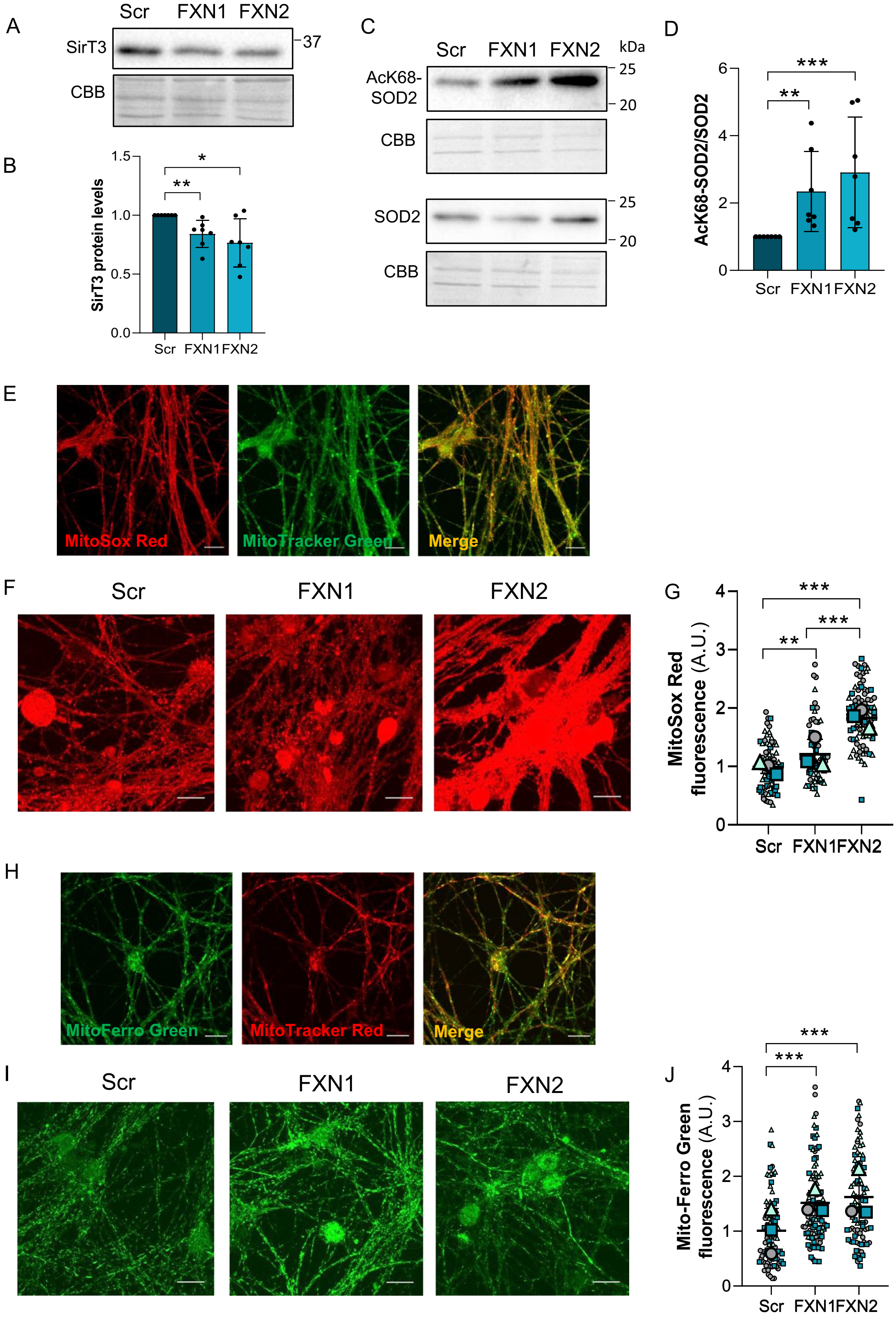
A
Scr
FXN1
FXN2
SirT3
37
CBB
B
SirT3 protein levels
1.5
1.0
0.5
0.0
*
**
Scr
FXN1
FXN2
C
Scr
FXN1
FXN2
kDa
AcK68-SOD2
25
20
CBB
SOD2
25
20
CBB
D
AcK68-SOD2/SOD2
6
4
2
0
***
**
Scr
FXN1
FXN2
E
MitoSox Red
MitoTracker Green
Merge
F
Scr
FXN1
FXN2
G
MitoSox Red fluorescence (A.U.)
4
3
2
1
0
***
***
**
Scr
FXN1
FXN2
H
MitoFerro Green
MitoTracker Red
Merge
I
Scr
FXN1
FXN2
J
Mito-Ferro Green fluorescence (A.U.)
4
3
2
1
0
***
***
Scr
FXN1
FXN2

◀ **Fig. 7** Oxidative stress increases in frataxin-deficient DRG primary cultures. **A** Western blot analysis SirT3 protein levels from frataxin-deficient DRG neurons (FXN1 and FXN2) compared to control cells (Scr) at day 5 after lentivirus transduction. CBB protein stain was used as a loading control. **B** Quantification data of A are mean ± SD obtained from n = 7 independent cultures. (**C**) SOD2 acetylated at Lys68 and total SOD2 were analyzed by western blot in Scr (control), FXN1 and FXN2 (5 days after lentivirus transduction) primary culture homogenates. Representative western blot images are shown. CBB protein stain was used as a loading control. **D** Histograms represent the mean ± SD from 7 independent isolations. Unpaired t test was performed (**B** and **D**). **E** A representative Z-stack image from DRG neurons, obtained by confocal microscopy, indicates the primarily mitochondrial localization of the fluorescent dye MitoSox Red using MitoTraker-Green as a mitochondrial control. Scale bar = 100 µm. **F** Mitochondrial superoxide levels were analyzed using MitoSox Red in frataxin-deficient DRG neurons (FXN1 and FXN2) and compared to control cells (Scr) at day 3 after lentivirus transduction. Scale bar = 100 µm. **G** Data are mean ± SD obtained from n = 3 independent isolations. Between 65 and 90 fields were analyzed for Scr, FXN1 and FXN2. For each condition, three images per field were taken. Kurskal-Wallis test with multiple pairwise-comparison corrected with Holm's method was applied. **H** Representative Z-stack image from DRG neurons, obtained by confocal microscopy, indicates the primarily mitochondrial localization of the fluorescent dye MitoFerro Green using Mitotracker-Red as a mitochondrial control. **I** Mitochondrial Fe.$^{2+}$ staining with Mito-FerroGreen probe in primary cultures of DRG neurons at day 3 after lentivirus transduction. Scale bar = 100 µm. **J** Data are mean ± SD obtained from n = 3 independent isolations. Between 88 and 104 fields were analyzed for Scr, FXN1 and FXN2. Kurskal-Wallis test with multiple pairwise-comparison corrected with Holm's method was applied. In **G** and **J**, each biological replicate is color-coded (day to day variability), and small symbols represent experimental replicates. Significant differences between Scr and FXN1 or FXN2 are indicated (p values < 0.05(*), 0.01(**), or 0.001(***))

Nevertheless, our NAD$^+$/NADH data are consistent with the reduced sirtuin activity observed. Since whole homogenates were used, we measured total sirtuin activity (NAD$^+$-independent deacetylase activities were fully inhibited). Among the seven sirtuins present in mammalian cells, extramitochondrial SirT1 and SirT2, and predominantly mitochondrial SirT3, showed the highest deacetylase activity [51], while other sirtuins performed deacetylation reactions other than acetyl groups (malonyl, succinyl, palmitoyl,…) and the ADP-ribosylation reaction [20]. Three sirtuins, SirT3, 4 and 5, are located predominantly within the mitochondrial matrix. SirT3 shows robust deacetylase activity while that of SirT4 and 5 is weak or null [19], 20. The results presented here showed a 40% decrease in total sirtuin activity in FXN1 cultures compared to Scr. This decrease was around 35–50% in total DRG homogenates from FXN^{I151F} mice compared to WT animals. These results indicate that: i) it is highly possible that in mitochondria the differences in SirT3 activity between mutant and WT animals could be higher; and ii) the impairment in the mitochondrial metabolism caused by frataxin deficiency probably disturbs the entire cell metabolism.

It has been reported that oxidative stress induces sirtuin levels [52] [53]. The SirT3 promoter has tandem Nrf2 consensus binding motifs [54] suggesting that Nrf2 regulates *SIRT3* expression and may explain *SIRT3* upregulation in response to various stressors. However, in the FA context, previously published results showed no differences in SirT3 protein levels in NSE-KO heart [40] or FXN-KO heart [39]. We observed moderate but significantly decreased SirT3 levels, both in FXN1 and FXN2 primary cultures, and DRGs from FXN^{I151F} mice (at 21 weeks of age) compared to controls. This decline may be due to (i) decreased synthesis, since reduced SirT3 mRNA expression was detected in FXN-KO heart [39]; or (ii) increased protein degradation after oxidative modification. In fact, SirT3 modification by 4-HNE was much higher in heart from frataxin-deficient mice compared to WT mice [40]. Such carbonyl group adduction has also been described in other pathological conditions, for example, in alcoholic liver disease [55], where the covalent modification of SirT3 by 4-HNE at Cys280 (a critical zinc-binding residue) was identified by tandem mass spectrometry. This modification resulted in the allosteric inhibition of SirT3 activity [55].

As already indicated, most of the available knowledge on SirT3 comes from studies in non-neuronal cells. Targets of SirT3 deacetylation have been analyzed in the heart [19], but the interactions between SirT3 and its protein substrates in the CNS are only just starting to be elucidated [51]. In DRGs from FA models, no information was available. In this work, acetylated proteins analyzed by western blot after one-dimensional SDS-PAGE showed a pattern with a predominant 52 kDa acetylated protein. This protein was identified by mass spectrometry after separation by 2D electrophoresis as alpha tubulin. Western blot anti acetyl-tubulin demonstrated increased alpha tubulin acetylation at 39 weeks of age, compared to WT mice. Tubulin, composed of heterodimers of alpha and beta tubulin, is the main component of microtubules, which play important roles in cell motility, mitosis, and intracellular vesicle transport. In fact, it has been described that frataxin deficiency leads to reduced growth cones in DRG of FA YG8sR model [56]. Tubulins are highly structured proteins, and both alpha and beta tubulin undergo many posttranslational modifications, including acetylation/deacetylation [41]. Neuronal alpha-tubulin acetylation occurs at Lys40 in the N-terminal region [57]. Tubulin acetylation level is a result of the balance between the activity of the cytoplasmic deacetylases HDAC6 and SirT2 [41] and mainly of the acetyltransferase MEC17 [42], which has been described to be increased in several models of FA [43]. In FXN^{I151F} mutant mice, we observed slightly decreased levels of SirT2 at 39 weeks of age, but not at 21 weeks. However, a clear induction of MEC17 was shown

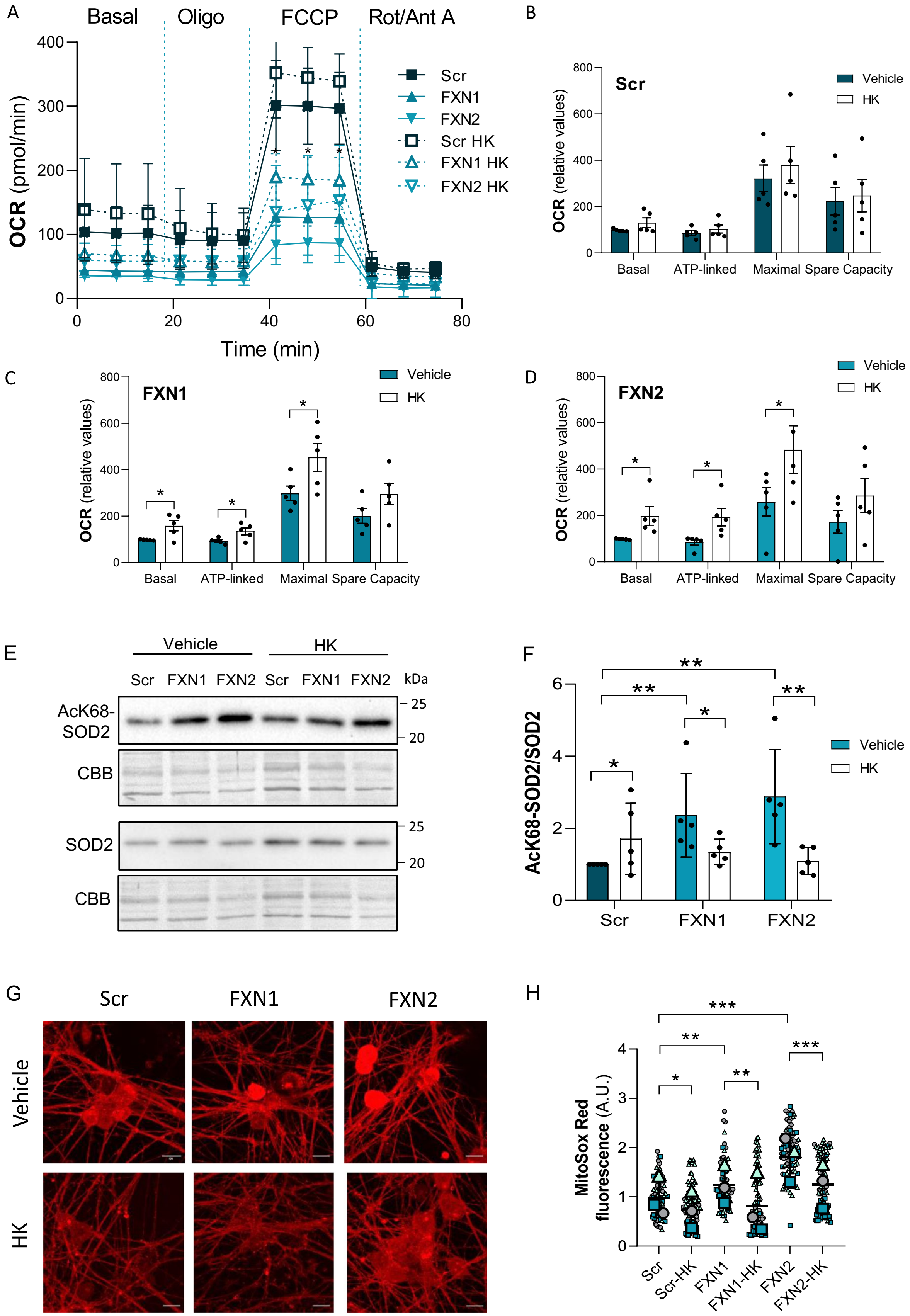
A
Basal
Oligo
FCCP
Rot/Ant A
OCR (pmol/min)
400
300
200
100
0
0
20
40
60
80
Time (min)
Scr
FXN1
FXN2
Scr HK
FXN1 HK
FXN2 HK
B
Scr
Vehicle
HK
OCR (relative values)
800
600
400
200
0
Basal
ATP-linked
Maximal
Spare Capacity
C
FXN1
Vehicle
HK
OCR (relative values)
Basal
ATP-linked
Maximal
Spare Capacity
D
FXN2
Vehicle
HK
OCR (relative values)
Basal
ATP-linked
Maximal
Spare Capacity
E
Vehicle
HK
Scr FXN1 FXN2 Scr FXN1 FXN2
kDa
AcK68-SOD2
CBB
SOD2
CBB
25
20
25
20
F
AcK68-SOD2/SOD2
6
4
2
0
Scr
FXN1
FXN2
Vehicle
HK
G
Scr
FXN1
FXN2
Vehicle
HK
H
MitoSox Red fluorescence (A.U.)
4
3
2
1
0
Scr
Scr-HK
FXN1
FXN1-HK
FXN2
FXN2-HK

◀**Fig. 8** Honokiol treatment ameliorated the impairment in oxygen consumption, SOD2 acetylation and superoxide levels detected in frataxin-deficient primary cultures. **A** Mitochondrial stress analysis of frataxin-deficient DRG neurons (FXN1 and FXN2) compared to control cells (Scr) at day 5 after lentivirus transduction (n = 5 independent cultures). Honokiol (2 µM) was added simultaneously with the virus (day 0) and 3 days later. **B**–**D** Basal respiration, ATP production, maximal respiration rate, and spare capacity of Scr cultures **B** compared to FXN1 **C** and FXN2 (**D**). Values are indicated as relative to basal respiration, and are mean ± SD obtained from n = 5 independent isolations. Unpaired t test was performed. **E** SOD2 acetylated at Lys68 and total SOD2 were analyzed by western blot in control (Scr) and frataxin-deficient DRG neurons (FXN1 and FXN2) at day 5 after lentivirus transduction. Honokiol (2 µM) was added as described above. Representative western blot images are shown. CBB protein stain was used as a loading control. **F** Histograms represent the mean ± SD from n = 5 independent isolations. Kurskal-Wallis test with Dunn's post-hoc correction was performed. **G** Mitochondrial superoxide levels were analyzed using the fluorescent dye MitoSox Red in frataxin-deficient DRG neurons (FXN1 and FXN2) and compared to control cells (Scr) at day 4 after lentivirus transduction. Honokiol (2 µM) was added as described above. Scale bar = 100 µm. **H** Data are mean ± SD obtained from n = 3 independent isolations. Between 65 and 95 soma were analyzed for Scr, FXN1 and FXN2. Each biological replicate is color-coded (day to day variability) and small symbols represent experimental replicates. Kurskal-Wallis test was performed with multiple pairwise-comparison corrected with Holm's method. Significant differences between Scr and FXN1 or FXN2 are indicated (p values < 0.05(*), 0.01(**), or 0.001(***))

in mutant mice compared to WT mice (at 21 and stronger at 39 weeks of age). The combination of decreased SirT2 and increased MEC17 can explain increased tubulin acetylation at 39 weeks. Reversible acetylation of alpha-tubulin may be involved in regulating microtubule stability, cell motility, and axon regeneration. However, the role of alpha-tubulin acetylation in neurons is very complex and not fully understood. On the one hand, it has been reported that Lys40 acetylation reduces the flexural rigidity of microfilaments, protecting them from damage after repetitive bending [58]. On the other hand, several reports have linked alpha-tubulin acetylation to neurodegeneration [59], 60. Moreover, microtubules play an important role in mitochondrial transport and the acetylation of tubulin also modulates mitochondrial length by affecting the transport activity of organelles and by modulating the interaction of mitofusin 2 with motor proteins [61]. At this point, the precise role that tubulin acetylation plays in the increased area and ultrastructural abnormalities observed in mitochondria of DRGs from the FXN^{I151F} mice would deserve future research.

Inside mitochondria, SirT3 activates the manganese-dependent SOD2 through deacetylation at the Lys68 site [62]. SOD2 is an essential antioxidant enzyme against the superoxide radicals generated inside mitochondria, mainly by the ETC. It has been reported to protect neurons against degeneration in several models of neurodegenerative disorders [63] [64]. We showed increased SOD2 acetylation at Lys68 in DRGs from the FXN^{I151F} mice. Interestingly, when compared to WT animals, a sixfold increase in acetylation was detected at 21 weeks of age while at 39 weeks, there was only a twofold increase. The opposite pattern was observed for alpha-tubulin, where the difference in acetylation versus the WT animals was higher at 39 weeks. This may indicate that mitochondrial SirT3 substrates are early targets while cytosolic proteins are acetylated later when the neurologic symptoms are evident. This boost in acetyl-SOD2 at 21 weeks would generate oxidative stress being more apparent at this initial stage of the disease. The amount of HNE bound to proteins is consistent with this idea, since levels in the mutant mice were higher at 21 weeks compared to 39 weeks. In agreement with our results, it has been reported that the SOD2 mutant mice (CD1-Sod2^{tm1Cje}) carrying inactive SOD2 exhibit inhibition of the respiratory chain complex I (NADH-dehydrogenase) and complex II (succinate dehydrogenase) [65].

By deacetylating SOD2, SirT3 protects neurons against metabolic and oxidative stress. It achieves this by reducing mitochondrial superoxide levels, stabilizing cellular and mitochondrial Ca^{2+} homeostasis, and inhibiting mitochondrial membrane transition pore opening to prevent apoptosis [66]. In primary cultures, we showed increased acetylation of SOD2 at Lys68 in FXN1 and FXN2 cells compared to Scr and a correlation with higher levels of superoxide anion in frataxin-deficient cells. In fact, previous results from our group also showed Ca^{2+} dyshomeostasis and MPTP opening in FXN1 and FXN2 primary cultures [11].

Honokiol is a biphenolic compound derived from the bark of magnolia trees and a widely known SirT3 activator. It has anti-inflammatory, anti-tumor, anti-oxidative, and neuroprotective properties [27]. Honokiol has shown some therapeutic effects in heart diseases, cancer, and metabolic diseases [67] but the mechanism(s) remains unclear. Honokiol enhances SirT3 expression and can be found in mitochondria [67] and a non-allosteric mechanism of activation of SirT3 has also been reported [68]. In the nervous system, honokiol has been reported to attenuate oxidative stress and neuroinflammation in the hippocampus [69]. It also mitigates oxidative stress and mitochondrial dysfunction by regulating mtROS homeostasis, partly via the AMPK/PGC-1α/SirT3 pathway [70]. In Alzheimer disease, honokiol increased SirT3 expression levels and activity, which in turn markedly improved ATP production and weakened mitochondrial ROS production, rescuing memory deficits [71]. When the compound was added to our primary cultures, an improvement in oxygen consumption was observed. The role of SirT3 in the mitochondrial dysfunction caused by frataxin deficiency was confirmed as honokiol treatment reduced both SOD2 acetylation and superoxide levels in FXN1 and FXN2 cells, which would improve mitochondrial fitness. It should be noted that the recovery in oxygen consumption was partial, but acetylated SOD2 and superoxide levels were decreased close to that of the control cells. This indicates that honokiol may have been able to almost fully recover SirT3 activity to WT levels, but other pathological alterations may also be relevant in mitochondrial impairment, including a deficit in Fe-S cluster biosynthesis and iron accumulation.

Although it remains a matter of debate, deficiency of Fe-S clusters could be a secondary trait in frataxin-deficient cells because FXN^{I151F} mice do not present a general loss of Fe-S clusters [29], and similar results were observed in the yeast model of FA [72]. Iron is the most abundant transition metal element within an organism, but because of its high reactivity, free iron and especially the reduced form ferrous ion, can catalyze the Fenton reaction, generating the highly reactive hydroxyl radical. Using the probe Mito-FerroGreen we demonstrated that frataxin-deficient DRG primary cultures accumulated mitochondrial Fe^{2+} compared to control cultures. A recent report described several conserved amino acid residues in the frataxin proteins, grouped in four clusters. It was hypothesized that cluster 3, present only in eukaryotic and Rickettsia frataxins but not in their bacterial homologs, may help to prevent the formation of ROS during iron detoxification [73]. Altogether this raises the possibility that ferroptosis may play a role in cellular death in sensory neurons, as has been described in several models of FA [13], 14. Although the increase in HNE-protein adducts suggests such a possibility, this hypothesis will need to be explored further.

In general, the two models used in this study show similar results and help us to understand the molecular effects (mainly in the mitochondria) of frataxin reduction in DRG sensory neurons. However, their differences can also give us some information. Primary cultures of rat DRG neurons are almost free of glial cells and FXN1 and FXN2, with 20–30% frataxin levels compared to Scr, show a highly impaired mitochondrial metabolism (Fig. 1). However, DRGs isolated from the mutant mice, which present only ~ 5% of frataxin levels compared to WT mice, have a milder mitochondrial decrease in ETC activity and a lower reduction in the NAD^+/NADH ratio compared to the primary culture model. This may be explained because (i) DRGs from mice have glial and systemic support that may help to prevent neurodegeneration; and (ii) primary cultures came from neonatal rats and isolated DRGs from adult mice (different species and time points). Differences between species are common, e.g., the requirement for frataxin seems to be much higher in humans than in mice; FA patients with residual frataxin levels of ~ 25% show a severe phenotype and decrease lifespan, but the KIKO mice model, with a similar percentage of frataxin, does not show motor deficits, iron accumulation or cardiac problems [74]; and (iii) the effect of the point mutation (Ile151 to Phe) on frataxin activity. Although we do not know whether this change might affect frataxin function, information based on human patients and mice models suggests that this mutation is probably neutral with respect to frataxin activity. Patients that are compound heterozygotes displaying GAA repeats on one allele and the I154F point mutation on the other show a classical phenotype, which is practically indistinguishable from those with triplet expansions in homozygosis, with similar frataxin levels in both cases. A new FA mouse model (YG8-800), which has 800 GAA repeats on both alleles, has been recently published [75] [76]. YG8–800 mice have around 1–15% frataxin levels compared to WT mice, similar to those found in the FXN^{I151F} mouse model and present a phenotype close to that shown by FXN^{I151F} [29].

Conclusions

The lack of frataxin induces, probably in multiple ways, a decrease in ETC and ATP synthesis, with the presence of morphologically abnormal mitochondria. Such mitochondrial dysfunction reduced the NAD^+/NADH ratio leading to lower sirtuin activity. We have provided evidence that the decrease in SirT3, a key regulator of mitochondrial energetic and antioxidant metabolism, resulted in oxidative stress due to increased SOD2 acetylation, which inactivates the enzyme. As a consequence, higher levels of superoxide in the mitochondria were detected, as well as increased HNE (a lipid peroxidation byproduct). In parallel with the frataxin deficiency, this may explain the Fe^{2+} accumulation, which exacerbates the oxidative stress. The role of SirT3 was demonstrated by honokiol treatment, which partially rescued the mitochondrial oxygen consumption deficits and almost completely rescued SOD2 acetylation and superoxide accumulation. We propose that because neurons have a high energy requirement, and fewer antioxidant systems compared to other tissues, the decay in the ETC results in decreased SirT3 activity and protein hyperacetylation, thus comprising a negative feedback contributing to neuron lethality.

Supplementary Information The online version contains supplementary material available at https://doi.org/10.1007/s00018-023-05064-4.

Acknowledgements We thank Roser Pané for her excellent technical assistance and Anaïs Panosa, from the Microscopy facility of University of Lleida, for helping in confocal imaging. We thank Anna Casanovas for her excellent teaching in the procedure of DRG extraction, and Josep Esquerda for his expertise and advise in electron microscopy imaging. We are also grateful to Ester Vilaprinyó for her assistance in the statistical analyses.

Author contributions Conceptualization, design and perform experiments: AS-A, FD, JT, MM-C, MP-G and EC. Data analysis: AS-A, JR, and EB. Histochemical examinations: AS-A, MP-C. Primary cell cultures and mice control: AS-A, MP-C, and FD. Writing original draft: AS-A, JR and EC. Reviewed and editing: JT, FD, JR and

EC. All authors have read and agreed to the published version of the manuscript.

Funding Open Access funding provided thanks to the CRUE-CSIC agreement with Springer Nature. This work was supported by: 1) Project PID2020-118296RB-I00 funded by MICIU/AEI /10.13039/501100011033; 2) Project CPP2021-008554 funded by MICIU/AEI /10.13039/501100011033 and by the European Union NextGenerationEU/ PRTR; 3) Project PDC2021-120758-I00 funded by MICIU/AEI /10.13039/501100011033 and by the European Union NextGenerationEU/ PRTR; 4) Project 2021-SGR 00323 funded by Generalitat de Catalunya. ASA received a Ph.D. fellowship from the Generalitat de Catalunya. Maria Pazos received a PhD fellowship from the Universitat de Lleida.

Data availability All data required to evaluate the conclusions in the paper are present in the manuscript and the supplementary materials.

Declarations

Conflict of interest The authors have no relevant financial or non-financial interests to disclose.

Ethical approval Animal use and care protocol conforms to the National Guidelines for the regulation of the use of experimental laboratory animals from the Generalitat de Catalunya and the Government of Spain (article 33.a 214/1997) and was evaluated and approved by the Experimental Animal Ethical Committee of the University of Lleida (CEEA).

References

1. Campuzano V, Montermini L, Moltò MD et al (1996) Friedreich's ataxia: autosomal recessive disease caused by an intronic GAA triplet repeat expansion. Science 271:1423–1427. https://doi.org/10.1126/SCIENCE.271.5254.1423
2. Galea CA, Huq A, Lockhart PJ et al (2016) Compound heterozygous FXN mutations and clinical outcome in friedreich ataxia. Ann Neurol 79:485–495. https://doi.org/10.1002/ANA.24595
3. Gervason S, Larkem D, Mansour Ben A et al (2019) Physiologically relevant reconstitution of iron-sulfur cluster biosynthesis uncovers persulfide-processing functions of ferredoxin-2 and frataxin. Nat Commun. https://doi.org/10.1038/S41467-019-11470-9
4. Alsina D, Purroy R, Ros J, Tamarit J (2018) Iron in friedreich ataxia: a central role in the pathophysiology or an epiphenomenon? Pharmaceuticals. 11:89
5. Gottesfeld JM (2019) Molecular mechanisms and therapeutics for the GAA·TTC expansion disease Friedreich Ataxia. Neurotherapeutics 16:1032–1049. https://doi.org/10.1007/S13311-019-00764-X
6. Pandolfo M (1998) Molecular genetics and pathogenesis of Friedreich ataxia. Neuromuscul Disord 8:409–415. https://doi.org/10.1016/S0960-8966(98)00039-X
7. Simon D, Seznec H, Gansmuller A et al (2004) Friedreich ataxia mouse models with progressive cerebellar and sensory ataxia reveal autophagic neurodegeneration in dorsal root ganglia. J Neurosci 24:1987–1995. https://doi.org/10.1523/JNEUROSCI.4549-03.2004
8. Koeppen AH (2011) Friedreich's ataxia: pathology, pathogenesis, and molecular genetics. J Neurol Sci 303:1–12. https://doi.org/10.1016/J.JNS.2011.01.010
9. Koeppen AH, Becker AB, Qian J et al (2017) Friedreich Ataxia: developmental failure of the dorsal root entry zone. J Neuropathol Exp Neurol 76:969–977. https://doi.org/10.1093/JNEN/NLX087
10. Mincheva-Tasheva S, Obis E, Tamarit J, Ros J (2014) Apoptotic cell death and altered calcium homeostasis caused by frataxin depletion in dorsal root ganglia neurons can be prevented by BH4 domain of Bcl-x L protein. Hum Mol Genet 23:1829–1841. https://doi.org/10.1093/hmg/ddt576
11. Britti E, Delaspre F, Tamarit J, Ros J (2021) Calpain-inhibitors protect frataxin-deficient dorsal root ganglia neurons from loss of mitochondrial Na+/Ca2+ exchanger, NCLX, and apoptosis. Neurochem Res 46:108–119. https://doi.org/10.1007/s11064-020-03020-3
12. Jiang X, Stockwell BR, Conrad M (2021) Ferroptosis: mechanisms, biology and role in disease. Nat Rev Mol Cell Biol 22:266–282. https://doi.org/10.1038/S41580-020-00324-8
13. la Rosa P, Petrillo S, Fiorenza MT et al (2020) Ferroptosis in Friedreich's Ataxia: a metal-induced neurodegenerative disease. Biomolecules 10:1–15. https://doi.org/10.3390/BIOM10111551
14. Grazia Cotticelli M, Xia S, Lin D et al (2019) Ferroptosis as a novel therapeutic target for Friedreich's Ataxia. J Pharmacol Exp Ther 369:47–54. https://doi.org/10.1124/JPET.118.252759
15. Purroy R, Britti E, Delaspre F et al (2018) Mitochondrial pore opening and loss of Ca2 + exchanger NCLX levels occur after frataxin depletion. Biochim Biophys Acta Mol Basis Dis 1864:618–631. https://doi.org/10.1016/j.bbadis.2017.12.005
16. Jiang D-Q, Wang Y, Li M-X et al (2017) SIRT3 in neural stem cells attenuates microglia activation-induced oxidative stress injury through mitochondrial pathway. Front Cell Neurosci 11:7. https://doi.org/10.3389/fncel.2017.00007
17. Yang W, Nagasawa K, Münch C et al (2016) Mitochondrial sirtuin network reveals dynamic SIRT3-dependent deacetylation in response to membrane depolarization. Cell 167:985-1000.e21. https://doi.org/10.1016/J.CELL.2016.10.016
18. Schwer B, North BJ, Frye RA et al (2002) The human silent information regulator (Sir)2 homologue hSIRT3 is a mitochondrial nicotinamide adenine dinucleotide-dependent deacetylase. J Cell Biol 158:647–657. https://doi.org/10.1083/JCB.200205057
19. Parodi-Rullán RM, Chapa-Dubocq XR, Javadov S (2018) Acetylation of mitochondrial proteins in the heart: the role of SIRT3. Front Physiol. https://doi.org/10.3389/fphys.2018.01094
20. Bheda P, Jing H, Wolberger C, Lin H (2016) The substrate specificity of sirtuins. Annu Rev Biochem 85:405–429. https://doi.org/10.1146/annurev-biochem-060815-014537
21. Lombard DB, Alt FW, Cheng H-L et al (2007) Mammalian Sir2 homolog SIRT3 regulates global mitochondrial lysine acetylation. Mol Cell Biol 27:8807–8814. https://doi.org/10.1128/MCB.01636-07
22. Finley LWS, Haas W, Desquiret-Dumas V et al (2011) Succinate dehydrogenase is a direct target of sirtuin 3 deacetylase activity. PLoS One. https://doi.org/10.1371/JOURNAL.PONE.0023295
23. Hirschey MD, Shimazu T, Goetzman E et al (2010) SIRT3 regulates mitochondrial fatty-acid oxidation by reversible enzyme

deacetylation. Nature 464:121–125. https://doi.org/10.1038/NATURE08778

24. Verdin E, Hirschey MD, Finley LWS, Haigis MC (2010) Sirtuin regulation of mitochondria: energy production, apoptosis, and signaling. Trends Biochem Sci 35:669–675. https://doi.org/10.1016/J.TIBS.2010.07.003
25. Stram AR, Wagner GR, Fogler BD et al (2017) Progressive mitochondrial protein lysine acetylation and heart failure in a model of Friedreich's Ataxia cardiomyopathy. PLoS ONE 12:e0178354. https://doi.org/10.1371/journal.pone.0178354
26. Chen T, Li J, Liu J et al (2015) Activation of SIRT3 by resveratrol ameliorates cardiac fibrosis and improves cardiac function via the TGF-β/Smad3 pathway. Am J Physiol Heart Circ Physiol 308:H424–H434. https://doi.org/10.1152/AJPHEART.00454.2014
27. Reverdy C, Gitton G, Guan X et al (2022) Discovery of novel compounds as potent activators of Sirt3. Bioorg Med Chem 73:116999. https://doi.org/10.1016/J.BMC.2022.116999
28. Pillai VB, Kanwal A, Fang YH et al (2017) Honokiol, an activator of Sirtuin-3 (SIRT3) preserves mitochondria and protects the heart from doxorubicin-induced cardiomyopathy in mice. Oncotarget. 8:34082–34098. https://doi.org/10.18632/ONCOTARGET.16133
29. Medina-Carbonero M, Sanz-Alcázar A, Britti E et al (2022) Mice harboring the FXN I151F pathological point mutation present decreased frataxin levels, a Friedreich ataxia-like phenotype, and mitochondrial alterations. Cell Mol Life Sci 79:1–20. https://doi.org/10.1007/s00018-021-04100-5
30. Sleigh JN, West SJ, Schiavo G (2020) A video protocol for rapid dissection of mouse dorsal root ganglia from defined spinal levels. BMC Res Notes 13:1–6. https://doi.org/10.1186/S13104-020-05147-6/FIGURES/3
31. Britti E, Delaspre F, Sanz-Alcázar A et al (2021) Calcitriol increases frataxin levels and restores mitochondrial function in cell models of Friedreich Ataxia. Biochem J 478:1–20. https://doi.org/10.1042/BCJ20200331
32. Böhm M, Papezova H, Hansikova H et al (2007) Activities of respiratory chain complexes in isolated platelets in females with anorexia nervosa. Int J Eat Disord 40:659–663. https://doi.org/10.1002/EAT.20403
33. Shepherd D, Garland PB (1969) The kinetic properties of citrate synthase from rat liver mitochondria. Biochem J 114:597–610. https://doi.org/10.1042/BJ1140597
34. Vorgerd M, Schöls L, Hardt C et al (2000) Mitochondrial impairment of human muscle in Friedreich ataxia in vivo. Neuromuscul Disord 10:430–435. https://doi.org/10.1016/S0960-8966(00)00108-5
35. Bradley JL, Blake JC, Chamberlain S et al (2000) Clinical, biochemical and molecular genetic correlations in Friedreich's ataxia. Hum Mol Genet 9:275–282. https://doi.org/10.1093/HMG/9.2.275
36. Heidari MM, Houshmand M, Hosseinkhani S et al (2009) Complex I and ATP content deficiency in lymphocytes from Friedreich's ataxia. Can J Neurol Sci 36:26–31. https://doi.org/10.1017/S0317167100006260
37. Napoli E, Taroni F, Cortopassi GA (2006) Frataxin, iron-sulfur clusters, heme, ROS, and aging. Antioxid Redox Signal 8:506–516. https://doi.org/10.1089/ARS.2006.8.506
38. Stepanova A, Magrané J (2020) Mitochondrial dysfunction in neurons in Friedreich's ataxia. Mol Cell Neurosci 102:103419
39. Martin AS, Abraham DM, Hershberger KA et al (2017) Nicotinamide mononucleotide requires SIRT3 to improve cardiac function and bioenergetics in a Friedreich's ataxia cardiomyopathy model. JCI Insight 2:e93885. https://doi.org/10.1172/jci.insight.93885
40. Wagner GR, Pride PM, Babbey CM, Payne RM (2012) Friedreich's ataxia reveals a mechanism for coordinate regulation of oxidative metabolism via feedback inhibition of the SIRT3 deacetylase. Hum Mol Genet 21:2688–2697. https://doi.org/10.1093/hmg/dds095
41. Janke C, Magiera MM (2020) The tubulin code and its role in controlling microtubule properties and functions. Nat Rev Mol Cell Biol 21:307–326
42. Kim G-W, Li L, Ghorbani M et al (2013) Mice lacking α-tubulin acetyltransferase 1 are viable but display α-tubulin acetylation deficiency and dentate gyrus distortion. J Biol Chem 288:20334–20350. https://doi.org/10.1074/jbc.M113.464792
43. Tong WH, Maio N, Zhang DL et al (2018) TLR-activated repression of Fe-S cluster biogenesis drives a metabolic shift and alters histone and tubulin acetylation. Blood Adv 2:1146–1156. https://doi.org/10.1182/BLOODADVANCES.2018015669
44. Chen Y, Zhang J, Lin Y et al (2011) Tumour suppressor SIRT3 deacetylates and activates manganese superoxide dismutase to scavenge ROS. EMBO Rep 12:534–541. https://doi.org/10.1038/EMBOR.2011.65
45. Tamarit J, Britti E, Delaspre F et al (2021) Crosstalk between nucleus and mitochondria in human disease: Mitochondrial iron and calcium homeostasis in Friedreich ataxia. IUBMB Life. Blackwell Publishing Ltd, New York, pp 543–553
46. Llorens JV, Soriano S, Calap-Quintana P et al (2019) The role of iron in Friedreich's Ataxia: insights from studies in human tissues and cellular and animal models. Front Neurosci. https://doi.org/10.3389/FNINS.2019.00075
47. Lin H, Magrane J, Rattelle A et al (2017) Early cerebellar deficits in mitochondrial biogenesis and respiratory chain complexes in the KIKO mouse model of Friedreich ataxia. Dis Model Mech 10:1343–1352. https://doi.org/10.1242/DMM.030502
48. Vicente-Acosta A, Giménez-Cassina A, Díaz-Nido J, Loria F (2022) The smoothened agonist SAG reduces mitochondrial dysfunction and neurotoxicity of frataxin-deficient astrocytes. J Neuroinflammation. https://doi.org/10.1186/S12974-022-02442-W
49. Chandran V, Gao K, Swarup V et al (2017) Inducible and reversible phenotypes in a novel mouse model of Friedreich's ataxia. Elife. https://doi.org/10.7554/ELIFE.30054
50. Murugasamy K, Munjal A, Sundaresan NR (2022) Emerging roles of SIRT3 in cardiac metabolism. Front Cardiovasc Med. https://doi.org/10.3389/FCVM.2022.850340/FULL
51. Sidorova-Darmos E, Sommer R, Eubanks JH (2018) The role of SIRT3 in the brain under physiological and pathological conditions. Front Cell Neurosci. https://doi.org/10.3389/fncel.2018.00196
52. Sorolla MA, Nierga C, José Rodríguez-Colman M et al (2011) Sir2 is induced by oxidative stress in a yeast model of Huntington disease and its activation reduces protein aggregation. Arch Biochem Biophys 510:27–34. https://doi.org/10.1016/j.abb.2011.04.002
53. Sundaresan NR, Samant SA, Pillai VB et al (2008) SIRT3 is a stress-responsive deacetylase in cardiomyocytes that protects cells from stress-mediated cell death by deacetylation of Ku70. Mol Cell Biol 28:6384–6401. https://doi.org/10.1128/MCB.00426-08
54. Satterstrom FK, Swindell WR, Laurent G et al (2015) Nuclear respiratory factor 2 induces SIRT3 expression. Aging Cell 14:818–825. https://doi.org/10.1111/ACEL.12360
55. Fritz KS, Galligan JJ, Smathers RL et al (2011) 4-Hydroxynonenal inhibits SIRT3 via thiol-specific modification. Chem Res Toxicol 24:651–662. https://doi.org/10.1021/tx100355a
56. Muñoz-Lasso DC, Mollá B, Sáenz-Gamboa JJ et al (2022) Frataxin deficit leads to reduced dynamics of growth cones in dorsal root ganglia neurons of friedreich's ataxia yg8sr model: a multilinear algebra approach. Front Mol Neurosci. https://doi.org/10.3389/FNMOL.2022.912780
57. Eddé B, Rossier J, le Caer J et al (1991) A combination of posttranslational modifications is responsible for the production of

neuronal alpha-tubulin heterogeneity. J Cell Biochem 46:134–142. https://doi.org/10.1002/JCB.240460207

58. Portran D, Schaedel L, Xu Z et al (2017) Tubulin acetylation protects long-lived microtubules against mechanical ageing. Nat Cell Boil. https://doi.org/10.1038/ncb3481
59. Tseng JH, Xie L, Song S et al (2017) The deacetylase HDAC6 mediates endogenous neuritic Tau pathology. Cell Rep 20:2169–2183. https://doi.org/10.1016/J.CELREP.2017.07.082
60. Pandey UB, Nie Z, Batlevi Y et al (2007) HDAC6 rescues neurodegeneration and provides an essential link between autophagy and the UPS. Nature 447:859–863. https://doi.org/10.1038/NATURE05853
61. Waddell J, Banerjee A, Kristian T (2021) Acetylation in mitochondria dynamics and neurodegeneration. Cells. https://doi.org/10.3390/CELLS10113031
62. Lu J, Cheng K, Zhang B et al (2015) Novel mechanisms for superoxide-scavenging activity of human manganese superoxide dismutase determined by the K68 key acetylation site. Free Radic Biol Med 85:114–126. https://doi.org/10.1016/J.FREERADBIOMED.2015.04.011
63. Andreassen OA, Ferrante RJ, Dedeoglu A et al (2001) Mice with a partial deficiency of manganese superoxide dismutase show increased vulnerability to the mitochondrial toxins malonate, 3-nitropropionic acid, and MPTP. Exp Neurol 167:189–195. https://doi.org/10.1006/EXNR.2000.7525
64. Keller JN, Kindy MS, Holtsberg FW et al (1998) Mitochondrial manganese superoxide dismutase prevents neural apoptosis and reduces ischemic brain injury: suppression of peroxynitrite production, lipid peroxidation, and mitochondrial dysfunction. J Neurosci 18:687–697. https://doi.org/10.1523/JNEUROSCI.18-02-00687.1998
65. Melov S, Coskun P, Patel M et al (1999) Mitochondrial disease in superoxide dismutase 2 mutant mice. Proc Natl Acad Sci U S A 96:846–851. https://doi.org/10.1073/PNAS.96.3.846
66. Cheng A, Yang Y, Zhou Y et al (2016) Mitochondrial SIRT3 mediates adaptive responses of neurons to exercise and metabolic and excitatory challenges. Cell Metab 23:128–142. https://doi.org/10.1016/J.CMET.2015.10.013
67. Pillai VB, Samant S, Sundaresan NR et al (2015) Honokiol blocks and reverses cardiac hypertrophy in mice by activating mitochondrial Sirt3. Nature Commun. https://doi.org/10.1038/ncomms7656
68. Upadhyay A, Guan X, Munshi S, Chakrabarti R (2020) Nonallosteric sirtuin enzyme activation: characterization of hit compounds. BioRxiv. https://doi.org/10.1101/2020.04.17.045187
69. Ye JS, Chen L, Lu YY et al (2019) SIRT3 activator honokiol ameliorates surgery/anesthesia-induced cognitive decline in mice through anti-oxidative stress and anti-inflammatory in hippocampus. CNS Neurosci Ther 25:355–366. https://doi.org/10.1111/cns.13053
70. Wang D, Cao L, Zhou X et al (2022) Mitigation of honokiol on fluoride-induced mitochondrial oxidative stress, mitochondrial dysfunction, and cognitive deficits through activating AMPK/PGC-1α/Sirt3. J Hazard Mater. https://doi.org/10.1016/J.JHAZMAT.2022.129381
71. Li H, Jia J, Wang W et al (2018) Honokiol alleviates cognitive deficits of Alzheimer's disease (PS1V97L) transgenic mice by activating mitochondrial SIRT3. J Alzheimers Dis 64:291–302. https://doi.org/10.3233/JAD-180126
72. Alsina D, Ros J, Tamarit J (2018) Nitric oxide prevents Aft1 activation and metabolic remodeling in frataxin-deficient yeast. Redox Biol 14:131–141. https://doi.org/10.1016/J.REDOX.2017.09.001
73. Alves R, Pazos-Gil M, Medina-Carbonero M et al (2022) Evolution of an iron-detoxifying protein: eukaryotic and Rickettsia frataxins contain a conserved site which is not present in their bacterial homologues. Int J Mol Sci 23:13151. https://doi.org/10.3390/IJMS232113151
74. Miranda CJ, Santos MM, Ohshima K et al (2002) Frataxin knockin mouse. FEBS Lett 512:291–297. https://doi.org/10.1016/S0014-5793(02)02251-2
75. Gérard C, Archambault AF, Bouchard C, Tremblay JP (2023) A promising mouse model for Friedreich Ataxia progressing like human patients. Behav Brain Res 436:114107. https://doi.org/10.1016/J.BBR.2022.114107
76. Kalef-Ezra E, Edzeamey FJ, Valle A et al (2023) A new FRDA mouse model [Fxn null:YG8s(GAA) > 800] with more than 800 GAA repeats. Front Neurosci. https://doi.org/10.3389/FNINS.2023.930422